

Atomic force microscopy dynamic modes: modeling and applications

This article has been downloaded from IOPscience. Please scroll down to see the full text article.

2008 J. Phys.: Condens. Matter 20 225012

(<http://iopscience.iop.org/0953-8984/20/22/225012>)

View [the table of contents for this issue](#), or go to the [journal homepage](#) for more

Download details:

IP Address: 129.252.86.83

The article was downloaded on 29/05/2010 at 12:30

Please note that [terms and conditions apply](#).

Atomic force microscopy dynamic modes: modeling and applications

Yaxin Song¹ and Bharat Bhushan^{2,3}

¹ Belcan Engineering Group Inc./Caterpillar Champaign Simulation Center, 1901 South First Street, Champaign, IL 61820, USA

² Nanoprobe Laboratory for Bio- and Nanotechnology and Biomimetics, The Ohio State University, 201 W. 19th Avenue, Columbus, OH 43210, USA

E-mail: bhushan.2@osu.edu

Received 11 February 2008, in final form 26 March 2008

Published 15 May 2008

Online at stacks.iop.org/JPhysCM/20/225012

Abstract

This paper contains a review of the development in modeling and applications of atomic force microscopy (AFM) modes. AFM is commonly used for atomic and nano-scale surface measurement. Two operational modes of AFM exist: static mode and dynamic mode. In dynamic AFM mode, a cantilever is driven to vibrate by its holder or the sample. The changes of cantilever vibration parameters due to tip-sample interaction are used to reveal surface properties of samples. Analytical and numerical models that can accurately simulate surface-coupled cantilever dynamics are essential for explaining AFM scanning images and evaluating a sample's material properties. The objective of this paper is to categorize the existing AFM dynamic modes and measurement techniques in terms of cantilever deflection and excitation mechanism, summarize AFM cantilever models presented in the literature, and demonstrate the applications of these models in AFM mode simulations. Based on the relations between cantilever responses and tip-sample interaction, methods for quantitative evaluation of a sample's mechanical parameters are described.

Contents

1. Introduction	2	4. Applications of FE model in AFM mode simulations	18
1.1. Various AFM modes and measurement techniques	2	4.1. FFM profiling process simulation	18
1.2. Models for AFM cantilevers	5	4.2. Vibration analysis of AFM tapping mode in liquid	23
2. Analytical modeling of AFM tip-cantilever systems	8	5. Quantitative evaluation of sample's mechanical properties	25
2.1. Tip-sample interaction	8	6. Closure	27
2.2. Point-mass model	9	References	28
2.3. 1D beam model	10		
2.4. Pure torsional analysis of TR mode	11	Abbreviations	
2.5. Coupled torsional-bending analysis of TR and LE modes	13	AFAM	Atomic force acoustic microscopy
3. Finite element modeling of tip-cantilever systems	15	AFFM	Acoustic friction force microscopy
3.1. Finite element beam model	15	AFM	Atomic force microscopy
3.2. Modeling of tapping mode	17	AM-AFM	Amplitude modulation atomic force microscopy
3.3. Modeling of TR and LE modes	17	DOF	Degrees of freedom
		FE	Finite element
		FFM	Friction force microscopy
		FM-AFM	Frequency modulation atomic force microscopy

³ Author to whom any correspondence should be addressed.

FMM	Force modulation mode
FRF	Frequency response function
HOPG	Highly oriented pyrolytic graphite
LE mode	Lateral excitation mode
LFM	Lateral force microscopy
LM-AFM	Lateral force modulation atomic force microscopy
MP	Metal particle
NC-AFM	Non-contact atomic force microscopy
STM	Scanning tunneling microscopy
TM	Tapping mode
TR mode	Torsional resonance mode
UAFM	Ultrasonic atomic force microscopy

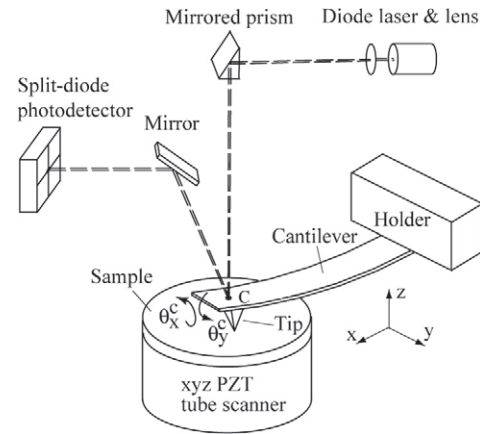


Figure 1. Schematic diagram of an AFM tip–cantilever assembly interacting with a sample surface. The four-segment photo-diode measures the flexural angle θ_y^C and twist angle θ_x^C of the cantilever.

1. Introduction

Atomic force microscopy (AFM) is commonly used for atomic and nano-scale measurement of various properties, including surface topography, friction, adhesion, and viscoelasticity (Bhushan 2005, 2007). During measurement, a micro-cantilever is scanned over a sample surface. Surface properties are revealed by observing the cantilever deflections or dynamic changes of vibration parameters (amplitude, resonance frequency, and phase angle) due to tip–sample interaction. Figure 1 shows the schematic diagram of an AFM tip–cantilever assembly interacting with a sample surface. The scanning is implemented by the motion of a cylindrical piezoelectric tube, which can act as the holder of either the cantilever or the sample. The deflection of the cantilever is measured using the optical lever method. A laser beam is projected on the upper surface of the cantilever close to the tip (point C). The reflected beam is led by a mirror into a four-segment photo-diode. The flexural angle (θ_y^C) and twist of the cantilever (θ_x^C) are obtained by calibrating the vertical and lateral voltage outputs of the photo-diode, respectively.

AFM cantilever deflection and vibration information under tip–sample interaction are utilized for surface topography, friction and material property imaging. For a quantitative explanation of these images and evaluation of material mechanical properties, the relationship between cantilever response and tip–sample interaction needs to be established. Analytical and numerical models that can accurately simulate the surface-coupled dynamics of the cantilever are essential for this purpose. In addition, a thorough understanding of cantilever dynamics is helpful for the development of AFM measurement techniques.

1.1. Various AFM modes and measurement techniques

Two types of micro-cantilevers are commonly used in AFM applications: rectangular and V-shaped cantilevers. Due to its geometric complexity, the calibration and modeling of a V-shaped cantilever is much more difficult than that of a rectangular cantilever. Since in practice rectangular cantilevers can perform at least equally well as V-shaped cantilevers, the universal use of rectangular cantilevers has been suggested by some researchers (Sader 2003, Sader and Sader 2003). In this

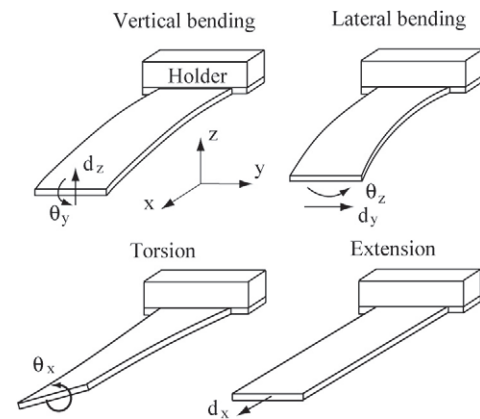
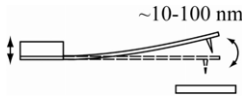

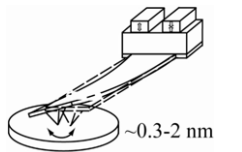
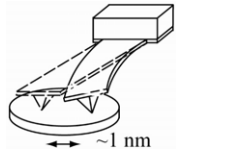
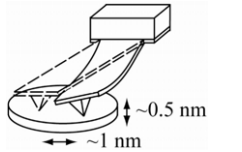


Figure 2. Four deformation shapes of a rectangular cantilever with free-clamped boundary conditions. Vertical bending is related to flexural angle θ_y and normal deflection d_z . Lateral bending is related to rotation angle θ_z and lateral deflection d_y . Twist angle θ_x is due to cantilever torsion. Extension causes the cantilever longitudinal displacement d_x .

review paper, we will confine our discussions to rectangular cantilevers.

A rectangular cantilever in AFM can be modeled as a three-dimensional (3D) beam with clamped–free boundary conditions. As shown in figure 2, the cantilever has four deformation shapes: vertical bending (bending about the y axis), lateral bending (bending about the z axis), torsion (about the x axis), and extension (along the x axis). Vertical bending is related to flexural angle θ_y and normal deflection d_z . Lateral bending is related to rotation angle θ_z and lateral deflection d_y . Twist angle θ_x is due to cantilever torsion. Extension causes the cantilever longitudinal displacement d_x . In terms of the cantilever state of motion during measurement, two basic types of AFM modes exist: static mode and dynamic mode. In static AFM modes, the cantilever is in quasi-static motion. In dynamic AFM modes, the cantilever is driven to vibrate near or at its resonance frequency, and then the cantilever tip is brought to the proximity of a sample surface for imaging. Compared to static AFM, dynamic AFM can provide a better signal-to-

Table 1. Summary of AFM modes.

Static modes						
Mode	Cantilever deflection	Output			Detected surface properties	
Contact mode	Vertical bending	Normal deflection			Topography, adhesion	
Friction force microscopy	Vertical bending, torsion and lateral bending	Normal deflection and twist angle			Topography, friction	
Dynamic modes						
Mode	Schematics	Cantilever deflection	Excitation source	Driving frequency	Output	Detected surface properties
Tapping mode, non-contact AFM		Vertical bending	Holder	Fundamental flexural resonance frequency	Normal deflection amplitude, phase and frequency shift	Topography and normal viscosity
Force modulation mode, atomic force acoustic microscopy mode		Vertical bending	Sample surface or holder	Fundamental and higher order flexural resonance frequency	Normal deflection amplitude and resonance frequency	Normal stiffness
Torsional resonance mode		Torsion and lateral bending	Holder	Torsional resonance frequency	Torsional amplitude, phase and resonance frequency	Topography, lateral stiffness and viscosity
Lateral excitation mode		Torsion and lateral bending	Sample surface	In a wide range, from very low (~20 kHz) to very high (up to 3 MHz)	Torsional amplitude, phase and resonance frequency	Topography, friction, lateral stiffness and viscosity
Combined normal and lateral excitation mode		Vertical bending, torsion and lateral bending	Sample surface	In vertical direction higher than first flexural resonance frequency; in lateral direction much lower than torsional resonance frequency	Normal deflection amplitude and phase, torsional amplitude, phase and resonance frequency	Normal stiffness and lateral stiffness

noise ratio and higher resolution in measurement of material and surface properties (Turner *et al* 1997, Dupas *et al* 2001, García and Pérez 2002).

Table 1 summarizes static and dynamic AFM modes. Static AFM modes include contact mode and friction force microscopy (FFM, or lateral force microscopy, LFM). In contact mode (MultiMode™ SPM Instructor Manual 1997), the cantilever tip is in constant contact with the sample surface.

The cantilever normal deflection is monitored from flexural angle θ_y^C . The normal tip-sample interaction force is calculated as the product of cantilever spring constant (stiffness of vertical bending) and normal deflection. By keeping a constant normal deflection through the z motion of the piezotube, the surface topography is tracked. If the cantilever is brought to the sample surface, pressed down and then pulled away, a force-distance curve can be obtained for adhesion measurement.

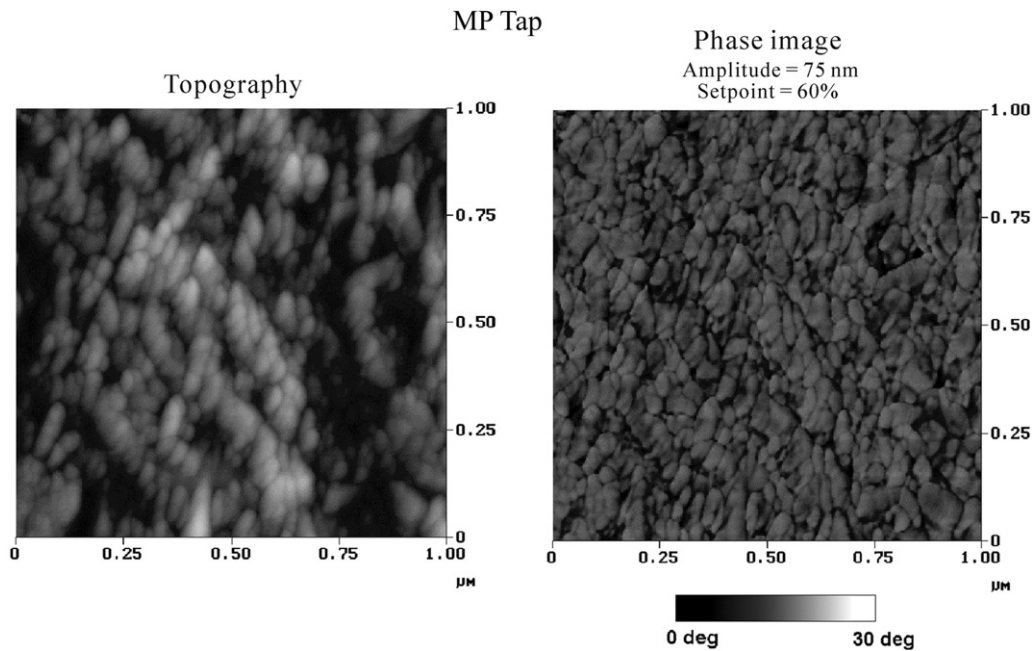


Figure 3. TM topography and phase angle images for MP tape. The setpoint is defined as the ratio of the cantilever vibration amplitudes after engagement to the free amplitude in air (Bhushan and Qi 2003).

FFM (Mate *et al* 1987, Marti *et al* 1990, Meyer and Amer 1990) is commonly used for friction measurement. In constant-force mode of FFM, a constant normal load is maintained, and the cantilever tip is scanned over sample surfaces. The scan direction is perpendicular to the longitudinal direction of the cantilever, and the friction force along that direction is obtained by measuring the cantilever twist angle.

Dynamic AFM modes considered here are categorized as the following types in terms of cantilever deflection and excitation mechanism: (1) tapping mode (TM), non-contact AFM (NC-AFM); (2) force modulation mode (FMM), atomic force acoustic microscopy (AFAM) mode (or ultrasonic atomic force microscopy, UAFM); (3) torsional resonance (TR) mode; (4) lateral excitation (LE) mode; (5) combined normal and lateral excitation mode.

In TM and NC-AFM, vertical bending dominates the cantilever deflection and the cantilever is excited by the vertical harmonic motion of its holder. TM is also named amplitude modulation AFM (AM-AFM). In TM, the cantilever is driven at a fixed frequency close or equal to the fundamental resonance frequency of vertical bending. During measurement, the vibrating tip touches the sample surface intermittently. The vibration amplitude is compared to the setpoint and the difference is used as a feedback parameter to track sample topography. The phase can be used for material viscosity imaging. Figure 3 shows the TM topography and phase angle images for a metal particle (MP) tape (Bhushan and Qi 2003). The topography and phase images show different characteristics. The phase image is correlated to the viscoelastic properties of the MP tape.

NC-AFM is also called frequency modulation AFM (FM-AFM) (Albrecht *et al* 1991). In NC-AFM, the cantilever is always oscillated at its resonance frequency with a constant

amplitude. During measurement, the vibrating tip does not touch the sample surface. Under the tip-sample interaction, the cantilever resonance frequency and oscillation amplitude are changing. A feedback loop detects the cantilever oscillation signal, shifts it by 90° , and uses it as the excitation signal so that the cantilever is always excited in resonance. Another feedback loop adjusts the excitation amplitude to keep the cantilever oscillating at a constant amplitude. In NC-AFM, the excitation signal is self-driven by the cantilever oscillation, which is dramatically different from the constant excitation used in TM. The spatial difference of frequency shift due to the tip-sample interaction can be used for contrast. The topography images are obtained by varying the tip-sample distance during the scan to keep a constant frequency shift. Compared to TM, NC-AFM can improve the imaging resolution dramatically by using a very high quality factor Q . Using NC-AFM, atomic resolution can be obtained by reducing the tip-sample distance and working in vacuum (Giessibl 1995, Kitamura and Iwatsuki 1995).

The dominant cantilever deflection in FMM and AFAM is vertical bending. In FMM and AFAM, the cantilever is driven to vibrate by the vertical motion of either the sample surface or the holder. During measurement, the cantilever tip is in constant contact with the sample surface and driven to vibrate vertically. The amplitude of the tip is kept as small as possible in order that the linear approximation of tip-sample forces is allowed, and to avoid lift-off. In FMM (Maivald *et al* 1991, Scott and Bhushan 2003), topography information is first obtained during primary scanning using TM. During interleaved scanning, the cantilever is moved up and down at the resonance frequency of the holder's bimorph (below the fundamental resonance of the cantilever). The z -direction feedback control is deactivated and the topography information

from the primary scan is used to maintain a constant lift scan height. The cantilever vibration amplitude can be used to image local stiffness. FMM can be used for elasticity contrast for soft materials such as polymers. For stiffer materials such as metals and ceramics, the contact stiffness between tip and surface is much higher than the spring constant of the cantilever (ranging from 0.01 to 80 N m⁻¹). The samples do not deform and thus the contrast due to elasticity becomes very low. In AFAM (Rabe and Arnold 1994, Yamanaka and Nakano 1996, Rabe *et al* 1996, 1998, 2000, 2002, Turner *et al* 1997, Amelio *et al* 2001, Hurley *et al* 2003, Turner 2004), the cantilever is driven at ultrasonic frequencies at the fundamental contact resonance and several other higher-order contact resonances. At higher-order modes, the effective stiffness of the cantilever is enhanced to deform the samples and sample elasticity can be evaluated.

In TR mode (Bhushan and Kasai 2004, Huang and Su 2004, Kasai *et al* 2004, Reinstädler *et al* 2005a), two piezoelectric elements are attached to the cantilever holder and vibrate out of phase to drive the cantilever into torsional oscillation. Under lateral (in-plane) tip-sample interaction, a lateral force and a torque are exerted on the cantilever, causing it to deflect in a combination of torsion and lateral bending. In LE mode (Yamanaka and Tomita 1995, Scherer *et al* 1999, Reinstädler *et al* 2003, 2005b, Caron *et al* 2004), the cantilever is driven to vibrate by the lateral oscillation of sample surfaces in a direction perpendicular to the longitudinal axis of the cantilever. As in TR mode, the cantilever in LE mode deflects in both torsion and lateral bending. Compared to other AFM modes such as TM, in which the tip-sample interaction is mainly in the normal direction, TR and LE modes were developed for in-plane surface property measurement. The properties of materials like thin films can be measured more readily with TR and LE modes. In addition, TR and LE modes have some inherent advantages in surface property imaging. (1) In TR and LE modes, the cantilever tip vibrates laterally (parallel) to the sample surface. During measurements, the tip remains close to the sample surface, ensuring more intensive tip-sample interaction and more surface material property-related information (Kasai *et al* 2004). (2) The torsional/lateral bending stiffness of a cantilever is typically two orders of magnitude higher than that of vertical bending. Therefore, most of the deformation in TR and LE modes occurs in the sample. TR and LE modes can be used to measure stiff and hard samples (Kasai *et al* 2004).

Two operation modes are possible for TR mode. In one mode, the cantilever is excited into torsional vibration and then approached to the sample surface. By keeping a constant torsional amplitude, surface topography can be measured from the z piezomotion (Huang and Su 2004, Kasai *et al* 2004). The then-obtained torsional phase data can be used for imaging of material viscoelasticity (Kasai *et al* 2004). In the second mode, the cantilever is pressed on the sample surface with a constant normal load and then driven to vibrate at a frequency equal or close to the torsional contact resonance frequency. The variation of resonance frequency, torsional amplitude, and phase angle are used for mapping of material properties (Chen and Bhushan 2005, Reinstädler *et al* 2005a). Figure 4 shows

the images of an MP tape using TM, TR mode I (constant amplitude) and TR mode II (constant deflection) (Chen and Bhushan 2005). Compared to the TM phase angle image, better contrast resulting from variations in viscoelasticity can be seen in the phase angle image using TR mode I. Amplitude and phase angle images using TR mode II have the largest contrast.

LE mode refers to the AFM measurement techniques in which the cantilever is driven by the lateral oscillation of sample surfaces through tip-sample interaction, such as lateral force modulation AFM (LM-AFM) (Yamanaka and Tomita 1995), acoustic friction force microscopy (AFFM) (Scherer *et al* 1999), and lateral atomic force acoustic microscopy (lateral AFAM) (Reinstädler *et al* 2003, 2005b, Caron *et al* 2004). The excitation frequency of sample surfaces could be in a wide range. In LM-AFM, the sample is laterally vibrated at a frequency (~ 16 kHz) well below the cantilever torsional/lateral bending resonance frequency. The torsional amplitude and phase are employed for friction imaging. In AFFM and lateral AFAM, the sample oscillates laterally at megahertz frequencies (up to 3 MHz) to excite the cantilever in torsional or lateral bending resonance. The torsional amplitude and contact resonance spectra are used for friction imaging. Compared with conventional FFM, the advantages of friction measurement using LE mode are that the topography-induced friction can be reduced significantly and friction measurement can be operated at higher relative velocities (of the order of 1 mm s⁻¹).

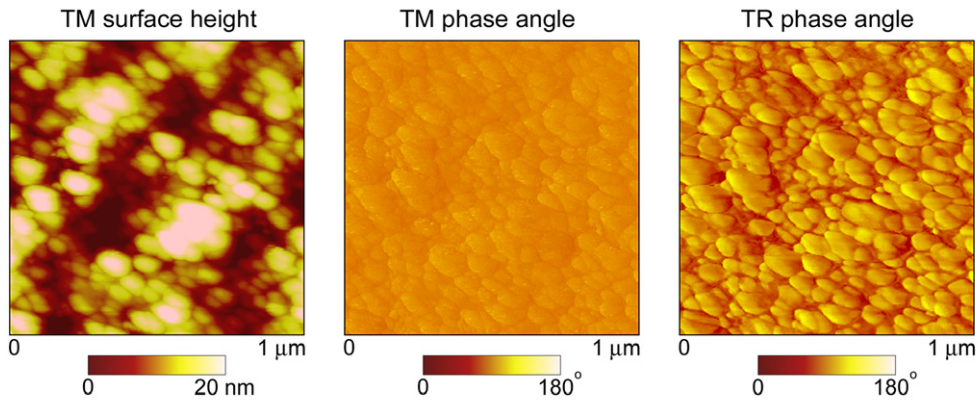
In combined normal and lateral excitation mode, which can be viewed as a combination of AFAM and LM-AFM, the cantilever is vertically excited by the sample surface at a frequency much higher than the flexural fundamental resonance frequency so that the tip is cyclically indented into the sample (Yamanaka *et al* 1994). At the same time, lateral oscillation of the surface at a frequency much lower than the cantilever torsional/lateral bending resonance frequency induces the cantilever vibration in torsional and lateral bending. By modulating the flexural vibration amplitude, subsurface features of normal stiffness can be imaged. The lateral stiffness of the subsurface can be imaged from the torsional responses of the cantilever.

1.2. Models for AFM cantilevers

Analytical and numerical models have been developed for dynamic simulation of AFM cantilevers with and without tip-sample interaction. Table 2 summarizes the AFM cantilever models for dynamic modeling.

Due to the existence of attractive and repulsive interaction regimes and the nonlinear nature of the normal tip-sample interaction forces, the dynamic behavior of a cantilever in TM and NC-AFM is very complicated. Point-mass models are employed in the investigation of cantilever dynamics in TM and NC-AFM. Point-mass models approximate the dynamics of the distributed-parameter cantilever system by the motion equation of a lumped mass. Using the point-mass models, researchers have obtained the analytical descriptions of nonlinear cantilever dynamics and provided insightful

TM surface height, TM phase angle and TR mode I phase angle images of MP tape
(Setpoint = 60%, TM amplitude in air = 20 nm, TR amplitude in air = 1 V)



TR mode II (constant deflection) surface height, amplitude and phase angle
images of MP tape (TR amplitude in air = 1 V, deflection = 25 nm)

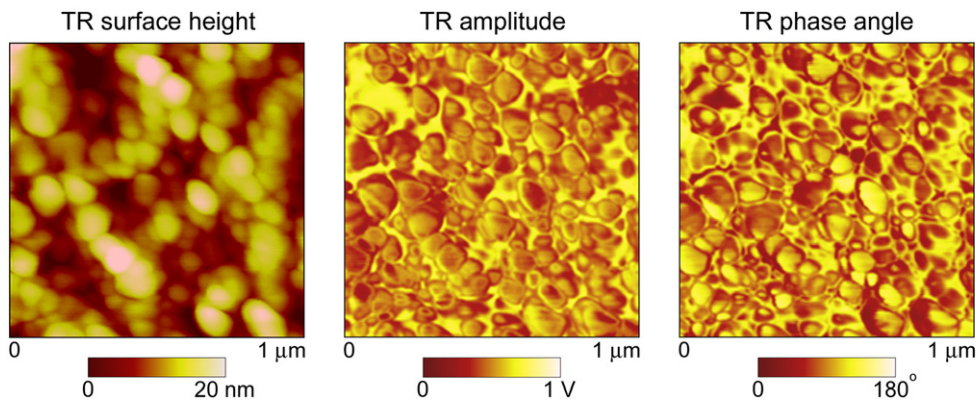


Figure 4. Images of MP tape using TM, TR mode I (constant amplitude) and TR mode II (constant deflection) (Chen and Bhushan 2005).

(This figure is in colour only in the electronic version)

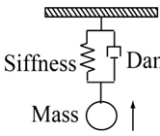
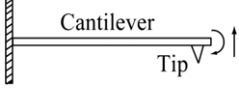
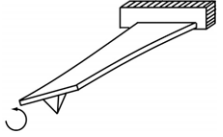
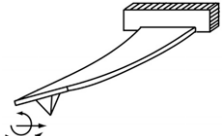
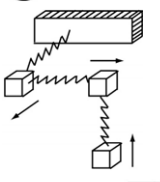
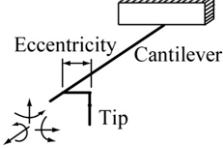
understanding of physical factors governing the motion of the cantilever (Chen *et al* 1994, Giessibl 1997, Wang 1998, 1999, San Paulo and García 2001).

It is recognized that in experiments higher-order flexural modes of the cantilever are often excited. Point-mass models cannot simulate the cantilever dynamics involving higher-order modes besides the fundamental one (Rabe *et al* 1996, Turner *et al* 1997, Stark *et al* 2004). Neither can point-mass models account for the effects of the geometry and location of the tip on the cantilever dynamics. Furthermore, point-mass models provide solutions corresponding to the cantilever vertical displacement while in experiment the detecting system of the AFM measures the rotation angle of the cantilever. This could give rise to some inaccuracy in data explanation since the vertical displacement and rotation angle of a vibrating cantilever do not have a one-to-one relation when higher modes of the cantilever are involved. One-dimensional (1D) beam models (Butt and Jaschke 1995, Rabe *et al* 1996, 1998, Lee *et al* 2002, Stark *et al* 2004) have been employed to investigate the cantilever response in TM and AFAM. Using the 1D beam models, analytical modal analyses of the tip–cantilever system were performed by representing the tip–sample interaction

by a linear spring and dashpot (Rabe *et al* 1996, Turner *et al* 1997, Wright and Nishiguchi 1997, Dupas *et al* 2001). This linearization is valid only if the tip oscillates around an equilibrium position with very small amplitudes. Considering the nonlinear Hertzian contact boundary conditions, the nonlinear amplitude–frequency relation for various flexural modes were obtained using the method of multi-scales (Turner 2004). In many cases, numerical methods, e.g. the finite element (FE) method (Arinero and L ev eque 2003, Song and Bhushan 2006b) or mode superposition method (Lee *et al* 2002, Stark *et al* 2004), are employed to simulate the nonlinear dynamics of a 1D beam.

In operation of TR and LE modes, the lateral oscillation of the cantilever tip over the sample surface is quite small (0.3–2 nm for TR mode and ~ 1 nm for LE mode). The tip–surface distance (therefore normal tip–sample force) remains almost constant, and the vertical deflection of the cantilever is uncoupled with the torsion and lateral bending. The dynamic response of the cantilever in TR and LE modes has been modeled as the pure torsional vibration of a shaft. Torsional modal analyses of the tip–cantilever system were performed with linear elastic tip–

Table 2. Summary of cantilever models for dynamic modeling.

Model	Schematics	Deflection modeled	Applications
1D point-mass model		Vertical bending	Non-contact mode, tapping mode
1D beam model		Vertical bending	Tapping mode, atomic force acoustic microscopy
Torsional model		Torsion	Torsional resonance mode, lateral excitation mode
Coupled torsional–bending model		Torsion and lateral bending	Torsional resonance mode, lateral excitation mode
3D point-mass model		3D translational displacements	Profiling process of friction force microscopy
3D finite element model		Vertical bending, torsion and lateral bending	Profiling process of friction force microscopy, all dynamic AFM modes

sample interaction (Yamanaka and Nakano 1998). The relation between the torsional amplitude/phase shift and lateral contact stiffness/viscosity in TR mode was derived in a forced torsional analysis (Song and Bhushan 2005, 2006a). The coupled torsional–bending model, which considers both the torsion and lateral bending of the cantilever in TR and LE modes, was developed recently (Song and Bhushan 2006c).

A 3D point-mass model (Hölscher *et al* 1996, 1997, 1998) was developed to simulate the tip motion during the profiling process of FFM. In the 3D point-mass model, the tip–cantilever system is represented by three masses connected by elastic springs to its holder. The point-mass model has three uncoupled translational degrees of freedom (DOFs). In each translational direction, the motion of the point mass is described as a single DOF oscillator. The friction force in this direction is obtained as the product of the translational displacement (relative to the holder) of the mass and the spring stiffness. As a mathematical approximation of the real tip–cantilever system, this model's parameters (effective masses and spring stiffnesses) can only be obtained by estimation, and the simulated responses are translational displacements instead of the rotation angles detected in FFM. The 3D point-mass model also neglects the coupling between the lateral bending and torsion of the cantilever.

The 3D FE beam model of tip–cantilever systems (Song and Bhushan 2006b) was developed for numerical simulation

of free (without tip–sample interaction) and surface-coupled (with tip–sample interaction) dynamics of AFM cantilevers in various dynamic modes. Representing the cantilever by 3D beam elements, this versatile model can address the exact excitation mechanisms, tip geometry/location, tilting of the cantilever to the sample surface, and all the possible couplings among the different deflections of the AFM cantilever. The FE model's parameters can be determined from the cantilever geometry and material properties. Translational displacements, as well as flexural and twist angles, are the simulated cantilever responses. The 3D FE beam model was used in the simulations of atomic-scale topographic and friction profiling process of FFM and AFM TM operated in liquid (Song and Bhushan 2006d, 2007).

In section 2, tip–sample interaction forces are described and analytical modeling techniques of AFM dynamic modes are investigated. In section 3, a 3D FE beam model is introduced for numerical simulation of free and surface-coupled dynamics of the tip–cantilever system in TM, TR and LE modes. In section 4, the 3D FE beam model is applied in simulations of the FFM profiling process and TM operated in liquid. In section 5, methods of evaluating the sample's mechanical properties from measured contact stiffness/viscosity are discussed. Section 6 concludes this paper.

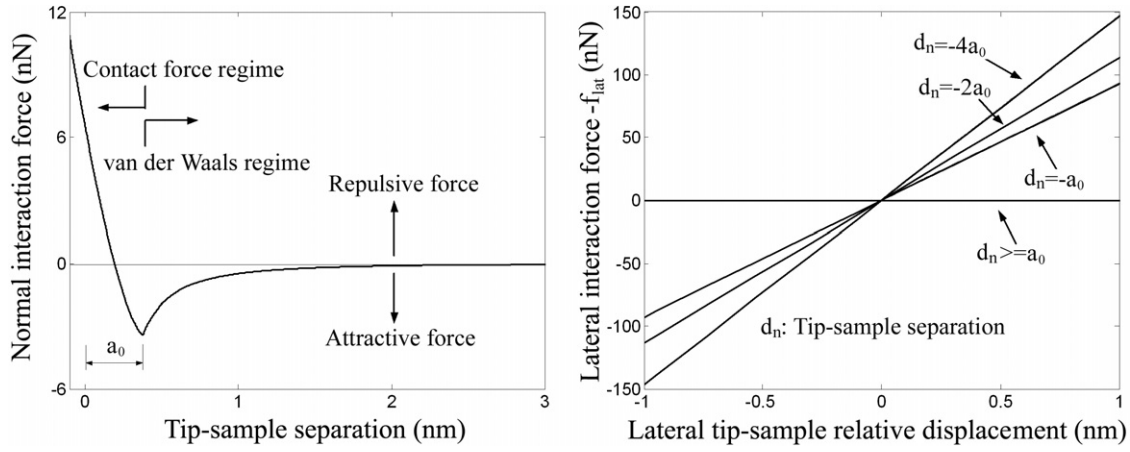


Figure 5. Normal interaction force described by van der Waals force and DMT contact force, and lateral interaction forces described by Hertzian contact theory.

2. Analytical modeling of AFM tip–cantilever systems

Analytical models have been developed for modeling AFM cantilever dynamics with and without tip–sample interaction. These models are used for various AFM modes with different cantilever deflections and excitation mechanisms. Cantilever responses, including contact resonance frequency, vibration amplitude and phase angle, have been used for material property imaging. The purpose of dynamic modeling of tip–cantilever systems is to investigate the relations between the cantilever responses and the tip–sample interaction. Tip–sample interaction is related to the sample’s material properties and the cantilever’s geometry and material properties. These derived relations between cantilever responses and tip–sample interaction can be used for a quantitative explanation of AFM images and the evaluation of a sample’s material properties. Modeling of cantilever dynamics also helps us understand the difference between cantilever behaviors and determine the application conditions of different dynamic modes.

2.1. Tip–sample interaction

To investigate the cantilever response during measurement, tip–sample interaction needs to be described first. The interaction between a cantilever tip and a sample can be modeled as the interaction between a sphere and a flat surface. Two different interaction regimes, attractive and repulsive, are distinguished in the normal direction of the cantilever. A van der Waals force is widely used to describe the long-range attractive force. Neglecting the energy dissipation in tip–sample contact, the short-range repulsive force in the normal direction can be calculated using the JKR (Johnson *et al* 1971) or DMT (Derjaguin *et al* 1975) model. The JKR model is suitable for soft, compliant materials with high adhesion forces and large tip radii, while the DMT model is suitable to describe the contact forces of hard, stiff materials with low adhesion forces and small tip radii. Adopting the DMT model, the

normal interaction force can be described as

$$f_n = \begin{cases} -\frac{HR}{6d_n^2}, & d_n > a_0 \\ -\frac{HR}{6a_0^2} + \frac{4}{3}E^*\sqrt{R}(a_0 - d_n)^{3/2} - \eta_n(a_0 - d_n)^{1/2}\dot{d}_n, & d_n \leq a_0. \end{cases} \quad (1)$$

Here, d_n is the transient tip–sample separation, H is the Hamaker constant, R is the tip radius, a_0 is the intermolecular distance, η_n is the viscosity of the tip–sample contact in the normal direction, ‘ $\dot{\cdot}$ ’ represents the differential with respect to time t , and E^* is the effective elastic modulus given by $E^* = [(1 - \nu_t^2)/E_t + (1 - \nu_s^2)/E_s]^{-1}$, where E_t , E_s , ν_t , and ν_s are the elastic moduli and Poisson’s ratios of the tip and sample, respectively.

According to the Hertzian contact theory (Johnson 1985), the tip–sample interaction force in the lateral direction is a function of the repulsive contact force, i.e.,

$$f_{lat} = \begin{cases} 0, & d_n > a_0 \\ -8G^* \left(\frac{3Rf_c}{4E^*}\right)^{1/3} \delta_{lat} - \eta_{lat}\dot{\delta}_{lat}, & d_n \leq a_0 \end{cases} \quad (2)$$

where $f_c = \frac{4}{3}E^*\sqrt{R}(a_0 - d_n)^{3/2}$ is the normal contact force, η_{lat} is the lateral viscosity of the tip–sample contact, δ_{lat} is the lateral relative displacement between the tip and sample, the effective shear modulus G^* is given by $G^* = [(2 - \nu_t)/G_t + (2 - \nu_s)/G_s]^{-1}$, and G_t and G_s are the shear moduli of the tip and sample.

Figure 5 shows the tip–sample interaction forces in normal and lateral directions between a cantilever and an HOPG (highly oriented pyrolytic graphite) sample. No energy dissipation due to the tip–sample interaction is considered ($\eta_n = 0$, $\eta_{lat} = 0$). The interaction in the normal direction is divided into two regimes. A negative value implies attractive force, whereas positive value represents repulsive force. The lateral interaction force is linearly proportional to lateral

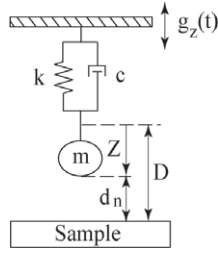


Figure 6. Schematic diagram of a point-mass model. The cantilever is excited to vibrate by the harmonic oscillation of the holder. D is the equilibrium tip-sample separation when the tip is far away from the sample when $g_z = 0$, Z is the spring deformation, and $d_n = D + Z + g_z(t)$ is the transient tip-sample separation.

relative displacement. The lateral contact stiffness depends on the normal contact force or tip-sample separation.

In the normal direction, if the cantilever is vibrating around an equilibrium position $d_n = D$ with very small amplitudes, the tip-sample interaction can be linearized using a linear viscoelastic model. The normal and lateral contact stiffnesses are determined by

$$k_n = -\left. \frac{\partial f_n}{\partial d_n} \right|_{d_n=D} = \begin{cases} -\frac{HR}{3D^3}, & d_n > a_0 \\ 2E^* \sqrt{R}(a_0 - D)^{1/2}, & d_n \leq a_0 \end{cases} \quad (3)$$

$$k_{lat} = -\left. \frac{\partial f_{lat}}{\partial \delta_{lat}} \right|_{d_n=D} = \begin{cases} 0, & d_n > a_0 \\ 8G^* \left(\frac{3Rf_c}{4E^*} \right)^{1/3}, & d_n \leq a_0. \end{cases} \quad (4)$$

In a repulsive regime ($d_n \leq a_0$), one may rewrite the normal and lateral contact stiffnesses as

$$k_n = 2a_c E^*, \quad (5)$$

$$k_{lat} = 8a_c G^* \quad (6)$$

where $a_c = \left(\frac{3Rf_c}{4E^*} \right)^{1/3}$ is the contact radius.

2.2. Point-mass model

Cantilever tip motion in AM-AFM and FM-AFM can be described by the point-mass model shown in figure 6. The cantilever holder is in a harmonic oscillation $g_z(t) = h_g \cos(\Omega t)$. The motion equation of the point mass is governed by a nonlinear second-order differential equation

$$m\ddot{Z} + c\dot{Z} + kZ = f_n - m\ddot{g}_z \quad (7)$$

where Z is the cantilever deflection, and m , c and k are the effective mass, viscous damping coefficient and spring constant of the cantilever, respectively. The effective mass can be obtained from $m = k/\omega_0^2$, where ω_0 is the fundamental natural frequency (in radians) of the cantilever. The damping coefficient is often expressed as $c = m\omega_0/Q$. The quality factor Q is a measure of the sharpness of the resonance spectra. Without tip-sample interaction, equation (7) is rewritten as

$$\ddot{Z} + \frac{\omega_0}{Q}\dot{Z} + \omega_0^2 Z = \Omega^2 h_g \cos(\Omega t). \quad (8)$$

The solution of equation (8) is

$$Z = A_t e^{-\omega_0 t/2Q} \sin\left(\sqrt{1 - (1/2Q)^2} \omega_0 t + \varphi_t\right) + A_0 \cos(\Omega t + \varphi). \quad (9)$$

The solution consists of an exponentially decaying transient term and a steady-state oscillation. After a time of $2Q/\omega_0$, the transient term decays by a factor of $1/e$. The steady-state oscillation has the same frequency Ω as the excitation. The amplitude and phase of the steady-state oscillation are expressed by

$$A_0 = \frac{h_g \Omega^2}{\sqrt{(\Omega^2 - \omega_0^2)^2 + (\Omega \omega_0/Q)^2}} \quad (10)$$

$$\varphi = \tan^{-1}\left(\frac{\Omega \omega_0}{Q(\Omega^2 - \omega_0^2)}\right). \quad (11)$$

When the driving frequency is equal to the resonance frequency of the undamped cantilever, $\Omega = \omega_0$, we have the relation

$$A_0 = Q h_g. \quad (12)$$

In AM-AFM, Wang (1998, 1999) applied the Krylov-Bogoliubov-Mitroposky asymptotic approximation to obtain the relations between oscillation response and normal interaction. A harmonic oscillation $Z = A_c \cos(\Omega t + \varphi) = A_c \cos \tilde{\theta}$ is assumed and the following relations are deduced:

$$A_c = \frac{h_g \Omega^2}{(1 + \tilde{\Omega}) \sqrt{\alpha_e^2 + (\tilde{\Omega} - \tilde{\omega}_e)^2}} \quad (13)$$

$$\varphi = \tan^{-1} \frac{\tilde{\omega}_e - \tilde{\Omega}}{\alpha_e} \quad (14)$$

where

$$\alpha_e = \alpha_0 + \frac{2}{\pi} \int_0^{\tilde{\theta}_0} \alpha_s \sin^2 \tilde{\theta} d\tilde{\theta} \quad (15)$$

$$\tilde{\omega}_e^2 = 1 + \frac{1}{\pi k A_c} \int_0^{\tilde{\theta}_0} f_n(A_c \cos \tilde{\theta}) \cos \tilde{\theta} d\tilde{\theta}. \quad (16)$$

Here, $\alpha_0 = 1/2Q$ is the damping of the cantilever, α_s is the damping from the normal interaction, $\tilde{\Omega} = \Omega/\omega_0$, $\tilde{\omega}_e$ is the normalized effective resonance frequency, and $\tilde{\theta}_0$ is determined from the contact position

$$\cos \tilde{\theta}_0 = \frac{D + a_0}{A_c}. \quad (17)$$

The phase angle measured in AM-AFM is related to the energy dissipation due to the tip-sample interaction (Cleveland *et al* 1998, Tamayo and García 1998). In the steady-state oscillation, the external energy supplied to the cantilever must equal the energy dissipated via tip-sample interaction (E_{dis}) and cantilever viscous damping in air. Under the assumption of a sinusoidal cantilever response, the following expression is obtained:

$$\sin \varphi = \frac{\Omega}{\omega_0} \frac{A_c(\Omega)}{A_0} + \frac{Q E_{dis}}{\pi k A_0 A_c(\Omega)} \quad (18)$$

where A_0 is the free amplitude and $A_c(\Omega)$ is the setpoint amplitude in AM-AFM.

In FM-AFM, the resonance frequency shift due to tip-sample interaction is utilized to produce surface images. In the case of small oscillation amplitude, the interaction can be approximated as a linear spring with stiffness k_n , as shown in equation (3). The resonance frequency of the point-mass system under tip-sample interaction is calculated by

$$\omega_c = \sqrt{\frac{(k + k_n)}{m}} = \omega_0 \sqrt{1 + \frac{k_n}{k}}. \quad (19)$$

Approximately, the frequency shift can be expressed as

$$\Delta\omega = \frac{\omega_c - \omega_0}{2\pi} \approx \frac{\omega_0}{2k} k_n. \quad (20)$$

In FM-AFM, the oscillation amplitudes are usually large compared to the tip-sample interaction range. Perturbation theory has to be employed to calculate the frequency shift. Using the first-order perturbation theory, Giessibl (1997) deduced the relation between frequency shift and the average work done by normal interaction force in a harmonic cycle

$$\Delta\omega = -\frac{\omega_0}{kA_c^2} \langle f_n z \rangle = -\frac{\omega_0}{kA_c^2} \int_0^{2\pi/\omega_0} f_n [d + A_c \cos(\omega_0 t)] A_c \cos(\omega_0 t) dt \quad (21)$$

where A_c is the set amplitude that the cantilever keeps during operation, and d is the closest distance of the tip to the sample.

Equations (13), (18) and (21) describe the relations of vibration amplitude, phase angle and frequency shift to normal tip-sample interaction in AM-AFM and FM-AFM, respectively. The vibration amplitude and frequency shift are both dependent on the average work done by the interaction force per period. The phase angle is related to the energy dissipation due to the tip-sample interaction.

2.3. 1D beam model

The 1D beam model shown in figure 7 is used in dynamic simulations of cantilever vertical bending in FMM and AFAM. The vertical bending of a cantilever is governed by the following ordinary differential equation (Gorman 1975):

$$EI_y \frac{\partial^4 w(x, t)}{\partial x^4} + \rho A \frac{\partial^2 w(x, t)}{\partial t^2} + c_{vb} \frac{\partial w(x, t)}{\partial t} = 0 \quad (22)$$

where $w(x, t)$ is the cantilever transverse displacement, E is the Young's modulus, ρ is the mass density, A is the cross section area, I_y is the moment of inertia about the y axis, $c_{vb} = \omega\rho A/Q$ is the damping coefficient for the cantilever when it is in vibrating in air, and ω is the natural frequencies of the cantilever corresponding to vertical bending. For a cantilever with a rectangular cross section, $I_y = bh^3/12$, where b and h are the width and thickness of the cross section, respectively.

It is assumed that the cantilever is a homogeneous, isotropic, linear elastic beam with a uniform cross section. In the modal analysis of free vibration, one seeks a solution as $w(x, t) = \phi_w(x)e^{i\omega t}$, where $i = \sqrt{-1}$. The modal shape function can be written as

$$\phi_w(x) = C_1 e^{-a_{vb}x} + C_2 e^{a_{vb}x} + C_3 e^{-ia_{vb}x} + C_4 e^{ia_{vb}x} \quad (23)$$

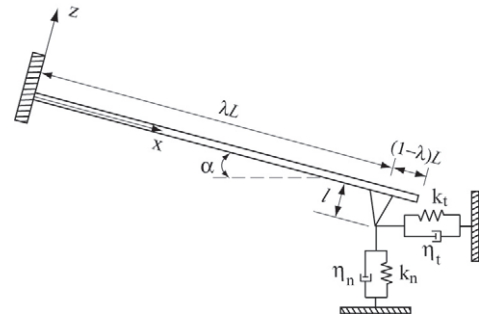


Figure 7. 1D beam model under linearized tip-sample interaction. The cantilever is tilted to the sample surface by an angle α . k_n , k_t , η_n and η_t are the contact stiffnesses and viscosities between the tip and surface in normal and in-plane directions, respectively.

where $a_{vb}^4 = \frac{\rho A}{EI_y} \omega^2 - i \frac{c_{vb}}{EI_y} \omega$, C_1 , C_2 , C_3 and C_4 are constants that can be determined by the following clamped-free boundary conditions:

$$\begin{aligned} \phi_w|_{x=0} = 0, \quad \phi'_w|_{x=0} = 0, \quad EI_y \phi''_w|_{x=L} = 0, \\ EI_y \phi'''_w|_{x=L} = 0 \end{aligned} \quad (24)$$

where L is the length of the cantilever, and superscript $'$ represents the first differential with respect to x .

By substituting equation (23) into the boundary conditions and enforcing the condition that the eigenvalue a_{vb} must take on values that ensure a nontrivial solution, a characteristic equation can be obtained to determine the resonance frequencies. For each resonance frequency, the corresponding modal shape is determined by solving the constants in equation (23) using (24). In the absence of damping, the characteristic equation is

$$1 + \cos(a_{vb}L) \cosh(a_{vb}L) = 0. \quad (25)$$

For a small oscillation around an equilibrium position, the normal and in-plane interaction can be represented by a linear spring and dashpot, as shown in figure 7. The modal analysis of the cantilever under linearized tip-sample interaction follows the same procedure as that for the cantilever without tip-sample interaction. Under the assumption that the tip is located at the end of the cantilever ($\lambda = 1$), the boundary conditions with interaction are

$$\begin{aligned} \phi_w|_{x=0} = 0, \quad \phi'_w|_{x=0} = 0, \quad EI_y \phi''_w|_{x=L} = F_x l, \\ EI_y \phi'''_w|_{x=L} = -F_z \end{aligned} \quad (26)$$

where l is the tip length, and F_x and F_z are the amplitudes of the harmonic interaction forces along the x and z axes of the cantilever. They are related to the amplitudes of the normal and in-plane interaction forces F_n and F_t , which are proportional to the amplitudes of the relative displacements between the tip and surface in the normal and in-plane directions (Δ_n and Δ_t)

$$F_n = -(k_n + i\omega\eta_n)\Delta_n, \quad F_{lat} = -(k_{lat} + i\omega\eta_{lat})\Delta_t \quad (27)$$

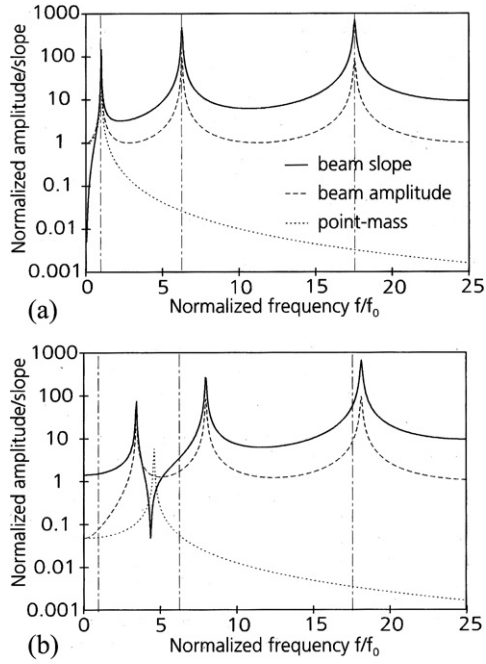


Figure 8. Forced vibration amplitude of cantilever deflection (dashed line) and rotation (solid line) compared with point-mass model (dotted line). (a) No tip-sample interaction. (b) $k_n/k = 20$, η_n is set as a small value, $k_t = 0$, $\eta_t = 0$ (Rabe *et al* 1998).

where Δ_n and Δ_t are obtained from the relative displacements Δ_x and Δ_z

$$\Delta_n = -\Delta_x \sin \alpha + \Delta_z \cos \alpha, \quad (28)$$

$$\Delta_t = \Delta_x \cos \alpha + \Delta_z \sin \alpha$$

$$\Delta_x = l\phi'_w|_{x=L}, \quad \Delta_z = \phi_w|_{x=L}. \quad (29)$$

Substituting equation (23) into equation (26), the characteristic equation to determine the contact resonance frequency of the cantilever under interaction can be obtained. Using the boundary conditions to solve the four constants in equation (23), modal shapes can be determined.

Forced vibration analysis can be carried out in a way similar to the above procedure. The excitation could be from the holder or from the sample surface. In both cases, the steady-state response of the cantilever can be assumed as $w(x, t) = \phi_w(x)e^{i\Omega t}$. With appropriate boundary conditions for each case, the cantilever response can be obtained. Figure 8 shows a comparison between the forced vibrations calculated from the 1D beam model and point-mass model (Rabe *et al* 1998). The first three free resonance frequencies are marked by the dashed vertical lines. Without tip-sample interaction, the point-mass model predicts well the vibration amplitude and the first resonance frequency. Due to the interaction, the spectral positions of resonances shift to higher values. The amplitude predicted by the point-mass model is orders of magnitude smaller and the contact resonance frequency predicted for the first mode is too high.

In AFAM, higher-order modes of the cantilever are excited for surface stiffness imaging. The sensitivities of frequency shift to variations in surface stiffness for each vibration mode are different. Neglecting the tilting of the cantilever ($\alpha = 0$)

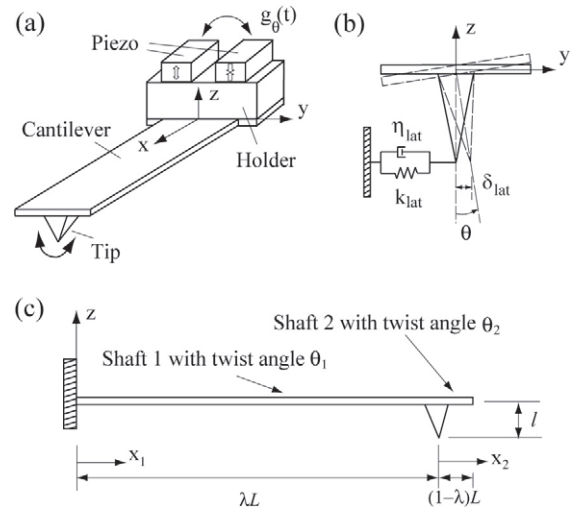


Figure 9. Schematic diagrams of a tip-cantilever assembly in TR mode. (a) The cantilever is excited into torsional vibration by the holder. (b) The cantilever under a linear viscoelastic interaction. (c) The tip is not located at the free end of the cantilever.

and contact damping, and assuming $k_t = 0$, a characteristic equation in the following form can be obtained:

$$\Pi(a_{vb}, k_n) = 0. \quad (30)$$

The derivative of the characteristic equation with respect to k_n yields

$$\frac{\partial a_{vb}}{\partial k_n} = -\frac{\partial \Pi / \partial k_n}{\partial \Pi / \partial a_{vb}}. \quad (31)$$

The sensitivity of frequency shift to surface stiffness can be obtained from

$$\frac{\partial \omega}{\partial k_n} = \frac{\partial \omega}{\partial a_{vb}} \frac{\partial a_{vb}}{\partial k_n}. \quad (32)$$

With a 1D beam model, a sensitivity study of flexural contact resonance frequency to normal surface stiffness can be carried out, and it shows that the first flexural mode is the most sensitive one for materials that are compliant relative to the cantilever stiffness. The higher-order vibration modes may be more sensitive than the first if the surface stiffness is high enough (Turner and Wiehn 2001).

2.4. Pure torsional analysis of TR mode

Figure 9 shows the tip-cantilever assembly in TR mode. The torsional vibration of the cantilever is governed by Gorman (1975)

$$GJ \frac{\partial^2 \theta(x, t)}{\partial x^2} = \rho I_p \frac{\partial^2 \theta(x, t)}{\partial t^2} + c_{tr} \frac{\partial \theta(x, t)}{\partial t} \quad (33)$$

where $\theta(x, t)$ is the rotation angle, G is the shear modulus, $c_{tr} = \omega \rho I_p / Q$ is the coefficient of viscous damping encountered by the cantilever when it is vibrating far away from sample surfaces, J is the torsional constant, and I_p is the polar area moment of inertia. For a cantilever with a

rectangular cross section,

$$J \approx \frac{1}{3}bh^3 \left[1.0 - 0.630\frac{h}{b} + 0.052 \left(\frac{h}{b}\right)^5 \right]$$

and $I_p = \frac{1}{12}(hb^3 + bh^3)$.

The torsional resonance frequency is $\omega\sqrt{1 - (1/2Q)^2}$, where ω is the resonance frequency in the absence of damping. Usually, damping in the cantilever is quite small. It has very little influence on the resonance frequencies of the system. The modal analysis can be made on the basis of no damping. Assuming a solution $\theta(x, t) = \Theta(x)e^{i\omega t}$ and substituting it into the governing equation, one obtains

$$\frac{d^2\Theta(x)}{dx^2} + \beta_\theta^2\Theta(x) = 0 \quad (34)$$

where $\beta_\theta^2 = \frac{\rho I_p}{GJ}\omega^2$. The modal shape function is

$$\Theta(x) = D_1 \sin(\beta_\theta x) + D_2 \cos(\beta_\theta x). \quad (35)$$

Considering the clamped and free boundary conditions

$$\Theta|_{x=0} = 0, \quad GJ\Theta'|_{x=L} = 0 \quad (36)$$

one can obtain the following characteristic equation:

$$\cos(\beta_\theta L) = 0. \quad (37)$$

The torsional mode shape for the cantilever is

$$\Theta(x) = C_0 \sin(\beta_\theta x) \quad (38)$$

where C_0 is an arbitrary constant.

With tip-sample interaction, the location of the tip on the cantilever becomes a factor affecting the dynamics of the system. Figure 9(c) shows a tip-cantilever system in which the tip is located away from the clamped end of the cantilever with a distance of λL ($0 < \lambda \leq 1$). The cantilever is modeled as two shafts with different twist angle functions, $\theta_1(x_1, t)$ ($0 \leq x_1 \leq \lambda L$) and $\theta_2(x_2, t)$ ($0 \leq x_2 \leq (1 - \lambda)L$). The modal shape functions for the two shafts are

$$\Theta_1(x_1) = D_1 \sin(\beta_\theta x_1) + D_2 \cos(\beta_\theta x_1) \quad (39)$$

$$\Theta_2(x_2) = D_3 \sin(\beta_\theta x_2) + D_4 \cos(\beta_\theta x_2) \quad (40)$$

where the constants D_1, D_2, D_3 and D_4 can be determined by two boundary conditions and two continuity conditions of the two shafts. Considering a linear elastic interaction, the characteristic equation to determine β_θ is (Song and Bhushan 2006a)

$$(\beta_\theta L) \cos(\lambda\beta_\theta L) + \sin(\lambda\beta_\theta L) \{ \chi_k - (\beta_\theta L) \times \tan[(1 - \lambda)\beta_\theta L] \} = 0 \quad (41)$$

where the dimensionless parameter $\chi_k = k_{lat}l^2L/(GJ)$ represents the relative stiffness ratio between tip-sample interface and the cantilever. The mode shapes of the two shafts are

$$\Theta_1(x_1) = C_0 \sin(\beta_\theta x_1) \quad (42)$$

$$\Theta_2(x_2) = C_0 \sin(\beta_\theta \lambda L) \{ \tan[\beta_\theta (1 - \lambda)L] \times \sin(\beta_\theta x_2) + \cos(\beta_\theta x_2) \}. \quad (43)$$

To establish the relation of torsional amplitude and phase angle with in-plane surface properties, forced torsional vibration analysis is needed. The holder vibrates harmonically with a circular frequency Ω as $g_\theta(t) = \theta_g e^{i\Omega t}$. The solutions for the two shafts are $\theta_1(x_1, t) = \Theta_1(x_1)e^{i\Omega t}$ and $\theta_2(x_2, t) = \Theta_2(x_2)e^{i\Omega t}$. Substitution of the solutions into the governing equation leads to

$$\frac{d^2\Theta_1(x_1)}{dx_1^2} + (\eta_\theta^2 - i\eta_c)\Theta_1(x_1) = 0 \quad (44)$$

$$\frac{d^2\Theta_2(x_2)}{dx_2^2} + (\eta_\theta^2 - i\eta_c)\Theta_2(x_2) = 0 \quad (45)$$

where $\eta_\theta^2 = \frac{\rho I_p}{GJ}\Omega^2$, $\eta_c = \frac{c_\pi}{GJ}\Omega$. The solutions of the above equations are

$$\Theta_1(x_1) = D_1 e^{-a_{tr}x_1} + D_2 e^{a_{tr}x_1} \quad (46)$$

$$\Theta_2(x_2) = D_3 e^{-a_{tr}x_2} + D_4 e^{a_{tr}x_2} \quad (47)$$

in which $a_{tr} = \sqrt{-\eta_\theta^2 + i\eta_c}$. The four constants in equations (46) and (47) can be determined by the following boundary and continuity conditions:

$$\Theta_1|_{x_1=0} = \theta_g, \quad GJ\Theta_2'|_{x_2=(1-\lambda)L} = 0 \quad (48)$$

$$\Theta_1|_{x_1=\lambda L} = \Theta_2|_{x_2=0},$$

$$GJ\Theta_1'|_{x_1=\lambda L} - GJ\Theta_2'|_{x_2=0} = -(k_{lat} + i\eta_{lat}\Omega)l^2\Theta_2|_{x_2=0}. \quad (49)$$

After obtaining the four constants D_1, D_2, D_3 and D_4 , one can calculate the torsion of the cantilever at the location of the tip as

$$\Theta_1(x_1 = \lambda L) = \Theta_2(x_2 = 0) = H_\theta(\Omega)\theta_g \quad (50)$$

where $H_\theta(\Omega)$ is the frequency response function (FRF) of the cantilever at the tip location (Song and Bhushan 2005).

The torsional magnitude and phase of the cantilever at the tip location are

$$A_\theta = |H_\theta(\Omega)|\theta_g \quad (51)$$

$$\phi = \text{Argument}[H_\theta(\Omega)]. \quad (52)$$

In dynamic AFM modes, phase shift is defined as the phase difference between the driving signal and cantilever response, which is $-\phi$ in this case. The phase shift $-\phi$ results from two sources. One is the phase shift due to the viscous damping encountered by the cantilever when it vibrates far away from the sample surface ($k_{lat} = 0$ and $\eta_{lat} = 0$). It is denoted as $-\phi_0$. The other is derived from the tip-sample interaction. If $k_{lat} = 0$ and $\eta_{lat} = 0$, the FRF of the cantilever at the location of the tip can be obtained as

$$H_\theta^0(\Omega) = \frac{e^{a_{tr}\lambda L} [e^{2a_{tr}(1-\lambda)L} + 1]}{(e^{2a_{tr}L} + 1)}. \quad (53)$$

The torsional magnitude and phase angle without interaction are $A_\theta^0 = |H_\theta^0(\Omega)|\theta_g$ and $\phi_0 = \text{Argument}[H_\theta^0(\Omega)]$.

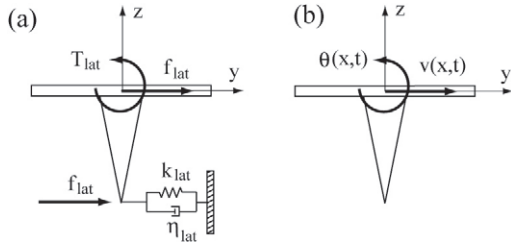


Figure 10. Schematic diagram of the cantilever tip under lateral tip-sample interaction. (a) The interaction is linear viscoelastic. A lateral force f_{lat} and a torque $T_{\text{lat}} = f_{\text{lat}}l$ are exerted on the cantilever. (b) The cantilever is under the deflections of lateral bending (lateral displacement $v(x, t)$) and torsion (twist angle $\theta(x, t)$).

2.5. Coupled torsional–bending analysis of TR and LE modes

As shown in figure 10, in TR and LE mode, the lateral force at the tip end causes the lateral bending and torsion of the cantilever. The torsion of the cantilever is governed by equation (33). The lateral bending is governed by the following ordinary differential equations:

$$EI_z \frac{\partial^4 v(x, t)}{\partial x^4} + \rho A \frac{\partial^2 v(x, t)}{\partial t^2} + c_{\text{lb}} \frac{\partial v(x, t)}{\partial t} = 0 \quad (54)$$

where $v(x, t)$ is the lateral displacement along the y axis, I_z is the moment of inertia about the z axis, and $c_{\text{lb}} = \omega_{\text{lb}} \rho A / Q$ are the damping coefficients for the lateral bending when the cantilever is vibrating in air. Here, ω_{lb} is the resonance frequency corresponding to lateral bending. For a cantilever with a rectangular cross section, $I_z = hb^3/12$.

In TR mode, assuming a harmonic motion of the holder as $g_\theta(t) = \theta_g e^{i\Omega t}$, one has $\theta(x, t) = \Theta(x) e^{i\Omega t}$ and $v(x, t) = \phi_v(x) e^{i\Omega t}$. Similarly, the lateral force and the relative displacement can be represented as $f_{\text{lat}} = F_{\text{lat}} e^{i\Omega t} \delta_{\text{lat}} = \Delta_{\text{lat}} e^{i\Omega t}$. Substituting the solutions into the governing equations for torsion and lateral bending, one has

$$\frac{d^2 \Theta(x)}{dx^2} - a_{\text{tr}}^2 \Theta(x) = 0 \quad (55)$$

$$\frac{d^4 \phi_v(x)}{dx^4} - a_{\text{lb}}^4 \phi_v(x) = 0 \quad (56)$$

where $a_{\text{tr}}^2 = -\frac{\rho l_p}{GJ} \Omega^2 + i \frac{c_{\text{tr}}}{GJ} \Omega$, $a_{\text{lb}}^4 = \frac{\rho A}{EI_z} \Omega^2 - i \frac{c_{\text{lb}}}{EI_z} \Omega$. The determination of the response functions $\Theta(x)$ and $\phi_v(x)$ requires two torsional-related and four lateral-bending-related boundary conditions. As shown in figure 11(a), the amplitude of relative displacement $\Delta_{\text{lat}} = l \Theta|_{x=L} + \phi_v|_{x=L}$. The six boundary conditions are

$$\Theta|_{x=0} = \theta_g, \quad (57)$$

$$GJ \Theta'|_{x=L} = -(k_{\text{lat}} + i\eta_{\text{lat}} \Omega) (l \Theta|_{x=L} + \phi_v|_{x=L}) l$$

$$\phi_v|_{x=0} = 0, \quad \phi_v'|_{x=0} = 0, \quad EI_z \phi_v''|_{x=L} = 0,$$

$$EI_z \phi_v'''|_{x=L} = (k_{\text{lat}} + i\eta_{\text{lat}} \Omega) (l \Theta|_{x=L} + \phi_v|_{x=L}). \quad (58)$$

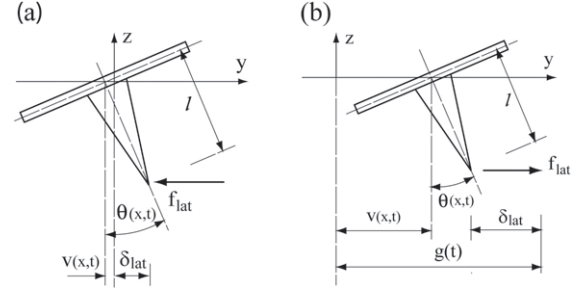


Figure 11. (a) Schematic diagrams of a cantilever deflection in TR mode. The cantilever is excited by the holder. (b) Schematic diagram of a cantilever deflection in LE mode. The cantilever is excited to vibrate by the harmonic oscillation of the sample surface through the lateral tip-sample interaction.

The response functions $\Theta(x)$ and $\phi_v(x)$ can be obtained by solving equations (55)–(58). The twist angle at the end of the cantilever is (Song and Bhushan 2006c)

$$\Theta_c \equiv \Theta(x = L) = \frac{2a_{\text{tr}} e^{a_{\text{tr}} L} GJ}{a_{\text{tr}} (e^{2a_{\text{tr}} L} + 1) GJ + (e^{2a_{\text{tr}} L} - 1) l^2 (k_{\text{lat}} + i\eta_{\text{lat}} \Omega) \gamma_c} \theta_g \quad (59)$$

in which

$$\gamma_c = \frac{a_{\text{lb}}^3 EI_z \pi_1}{a_{\text{lb}}^3 EI_z \pi_1 + (1 + i)(k_{\text{lat}} + i\eta_{\text{lat}} \Omega) \pi_2} \quad (60)$$

$$\pi_1 = 1 + e^{2ia_{\text{lb}} L} + 4e^{(1+i)a_{\text{lb}} L} + e^{2a_{\text{lb}} L} + e^{2(1+i)a_{\text{lb}} L} \quad (61)$$

$$\pi_2 = 1 - ie^{2ia_{\text{lb}} L} + ie^{2a_{\text{lb}} L} - e^{2(1+i)a_{\text{lb}} L}. \quad (62)$$

With the lateral bending being neglected, the cantilever would be in pure torsion and the twist angle at the end of the cantilever is

$$\Theta_p \equiv \Theta(x = L) = \frac{2a_{\text{tr}} e^{a_{\text{tr}} L} GJ}{a_{\text{tr}} (e^{2a_{\text{tr}} L} + 1) GJ + (e^{2a_{\text{tr}} L} - 1) l^2 (k_{\text{lat}} + i\eta_{\text{lat}} \Omega)} \theta_g. \quad (63)$$

Comparing Θ_c with Θ_p , we can see that Θ_c equals Θ_p only if the coupling coefficient $\gamma_c = 1$. This means that the lateral bending of the cantilever can be neglected if $\pi_1 \rightarrow \infty$, or $\pi_2 \rightarrow 0$, or the tip-sample interaction is very weak ($k_{\text{lat}} \rightarrow 0$ and $\eta_{\text{lat}} \rightarrow 0$).

In LE mode, the sample surface is oscillating in a harmonic motion expressed as $g(t) = a_g e^{i\Omega t}$. Compared to TR mode, in which the driving frequency has to be at or close to the cantilever torsional resonance frequency, in LE mode the driving frequency could be a value in a wide range. It could be much lower than the torsional/lateral bending resonance frequency of the cantilever, or very high around the aforementioned resonance frequency. As in TR mode, the cantilever undergoes a combination of torsion and lateral bending governed by equations (33) and (54). By assuming $\theta(x, t) = \Theta(x) e^{i\Omega t}$ and $v(x, t) = \phi_v(x) e^{i\Omega t}$, we have equations (55) and (56) to obtain the response functions $\Theta(x)$ and $\phi_v(x)$. As shown in figure 11(b), the relative displacement

Table 3. Relations of cantilever responses and tip-sample interaction in TR and LE modes.

	TR mode (excitation from the holder)		LE mode (excitation from the sample)	
	Twist angle	Lateral displacement	Twist angle	Lateral displacement
Weak interaction	Free amplitude	Zero	Zero	Zero
Increasing interaction	Decreasing	Increasing	Increasing	Increasing
Strong interaction	Zero	Maximum	Maximum	Maximum

amplitude $\Delta_{\text{lat}} = l\Theta|_{x=L} + \phi_v|_{x=L} - a_g$. The six boundary conditions are

$$\Theta|_{x=0} = 0,$$

$$GJ\Theta'|_{x=L} = -(k_{\text{lat}} + i\eta_{\text{lat}}\Omega)(l\Theta|_{x=L} + \phi_v|_{x=L} - a_g)l \quad (64)$$

$$\phi_v|_{x=0} = 0, \quad \phi_v'|_{x=0} = 0, \quad EI_z\phi_v''|_{x=L} = 0,$$

$$EI_z\phi_v'''|_{x=L} = (k_{\text{lat}} + i\eta_{\text{lat}}\Omega)(l\Theta|_{x=L} + \phi_v|_{x=L} - a_g). \quad (65)$$

The twist angle at the end of the cantilever is (Song and Bhushan 2006c)

$$\Theta_c \equiv \Theta(x=L) = \frac{a_g}{l + \frac{a_{\text{tr}}(e^{2a_{\text{tr}}L} + 1)GJ}{(e^{2a_{\text{tr}}L} - 1)(k_{\text{lat}} + i\eta_{\text{lat}}\Omega)l} \frac{1}{\gamma_c}}. \quad (66)$$

The pure torsional analysis of LE mode can be obtained by setting $\phi_v = 0$ and the twist angle at the end of the cantilever is

$$\Theta_p \equiv \Theta(x=L) = \frac{a_g}{l + \frac{a_{\text{tr}}(e^{2a_{\text{tr}}L} + 1)GJ}{(e^{2a_{\text{tr}}L} - 1)(k_{\text{lat}} + i\eta_{\text{lat}}\Omega)l}}. \quad (67)$$

Comparing Θ_c with Θ_p , we can see that, as in TR mode, Θ_c equals Θ_p only if the coupling coefficient $\gamma_c = 1$.

Due to the different excitation mechanisms, the cantilever response shows different characteristics in TR and LE modes. A detailed parameter analysis was performed by Song and Bhushan (2006c) to investigate these differences and under what conditions the pure torsional analysis is acceptable. Table 3 summarizes the cantilever responses to different tip-sample interactions in TR and LE modes.

In TR mode, excitation frequency is close to either the torsional resonance frequency or the torsional contact resonance frequency of the cantilever. In some cases of LE mode, such as AFFM and lateral AFAM, excitation frequency is around the cantilever torsional and lateral bending resonance frequencies, while in others, such as LM-AFM, very low frequency lateral force modulation is employed. Figure 12 (Song and Bhushan 2006c) shows the FRFs of torsional angles Θ_c and Θ_p , in TR mode and in LE mode. The FRFs of the torsional angle Θ_c in TR and LE modes can be calculated from equations (59) and (66) by setting the excitation amplitude $\theta_g = 1$ and $a_g = 1$, respectively. The FRFs of Θ_p can be obtained in the same way using equations (63) and (67).

In figure 12(a), it is clear that with no interaction the cantilever is in pure torsional vibration. With lateral tip-sample interaction, lateral bending is coupled with the torsion and the FRF resonances shift to the right. If a very low excitation frequency is used in TR mode, torsional vibration could hardly be excited. If the excitation frequency Ω is around

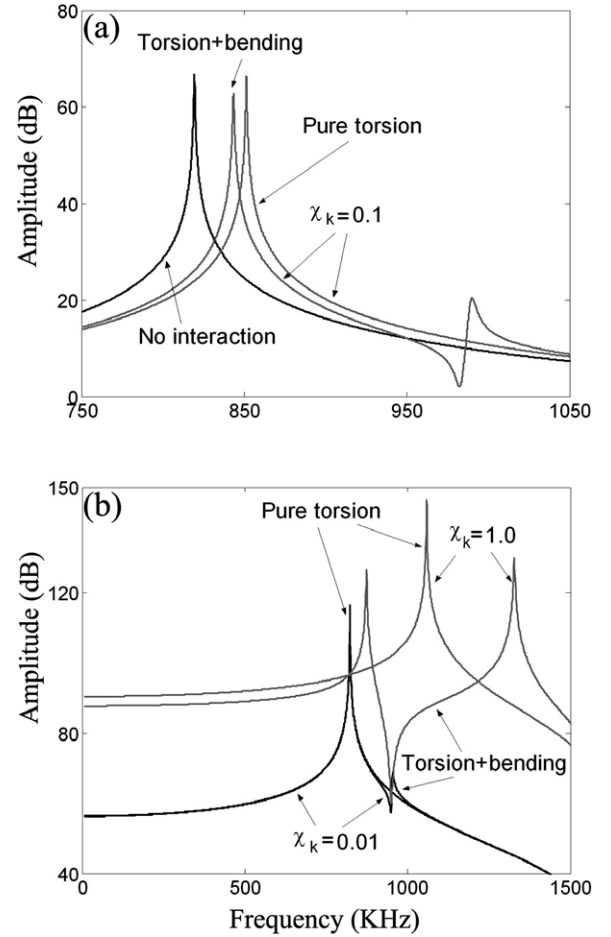


Figure 12. Frequency response functions of torsional angles Θ_c and Θ_p , in TR mode (a) and in LE mode (b). Lateral viscosity η_{lat} is neglected (Song and Bhushan 2006c).

the torsional resonance frequency ω_{tr} , even a medium lateral tip-sample interaction would result in a dramatic decrease in torsional amplitude. Therefore, $\Omega = \omega_{\text{tr}}$ is only suitable for measurement with relatively weak interaction. For medium lateral interaction, one could choose an excitation frequency that is close to the torsional contact resonance frequency so that a significant torsional angle can be measured. However, if the interaction is relatively strong, the cantilever has approximately clamped-clamped boundary conditions. Even at the torsional contact resonance, the torsional amplitude will not be big enough. Generally, the torsional amplitude corresponding to the lateral bending mode is rather small (see the small peak around 970 kHz in figure 12(a)). This means the contact resonance frequency of lateral bending may not be

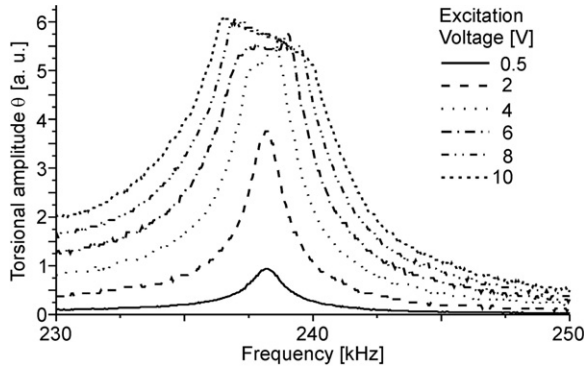


Figure 13. Torsional resonance curves of a cantilever measured on fused silica with different amplitudes of excitations (Reinstädler *et al* 2005b).

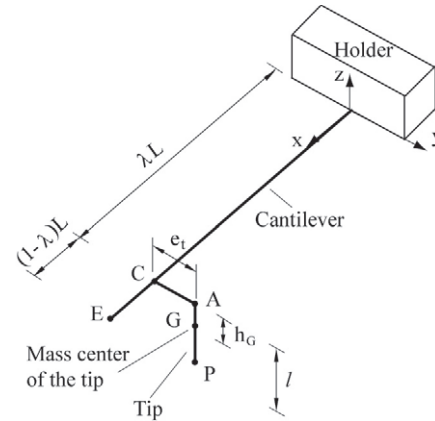


Figure 14. Schematic diagram of tip-cantilever system. The cantilever is represented by 3D beam elements and the tip by a rigid bar. The tip is not positioned perfectly on the central line of the cantilever.

Table 4. Summary of application conditions for TR and LE modes.

	Driving frequency	Applicable for
TR mode	Free torsional resonance	Weak interaction
	Contact torsional resonance	Weak or medium interaction
LE mode	Very low	Strong interaction
	Contact torsional resonance	Any interaction
	Contact resonance of lateral bending	Medium or strong interaction

used as the excitation frequency in TR mode. To sum up, TR mode might only be used for measurement of sample surface with relatively weak tip-sample interaction.

In figure 12(b), FRFs for LE mode are very different from those for TR mode. In LE mode, lateral tip-sample interaction always exists. As the interaction becomes stronger, the FRF resonance amplitude increases. If the excitation frequency is much lower than the torsional/lateral bending resonance frequency, torsional vibration can be significant only if the interaction is relatively strong, i.e., low frequency LM-AFM may be used only under relatively strong lateral tip-sample interaction. If the excitation frequency is around the torsional and lateral bending resonance frequencies, the torsional amplitude is increased. When the lateral interaction is relatively small the torsional amplitude corresponding to the lateral bending mode is quite small, but when the interaction becomes stronger it increases rapidly to the same order as that of the torsional mode. Therefore, for relatively weak tip-sample interaction the excitation frequency should be around the torsional resonance frequency, and for relatively strong tip-sample interaction both torsional and lateral bending modes may be excited for measurement. Table 4 summarizes the application conditions for TR and LE modes.

In the above analyses for TR and LE modes, it is assumed that there is no slip occurring between the tip and sample surface during measurement, i.e., the lateral interaction force does not exceed the critical friction force. This is the condition that must be satisfied so that the linear viscoelastic interaction model is valid. It is found that in TR and LE modes, under a certain applied normal load, a critical excitation amplitude, which indicates the onset of sliding

between the tip and sample, can be determined by observing the shape of the resonance curves (Reinstädler *et al* 2003). Torsional resonance curves measured with different amplitudes of excitation are shown in figure 13 (Reinstädler *et al* 2003). At low excitation amplitudes the shape of the resonance curve is Lorentzian. With the increasing of excitation amplitude, deviations from the Lorentzian shape appear. Above the critical excitation amplitude, the resonance curve flattens out and the frequency span of the flattened part increases with the excitation amplitude. By choosing an excitation amplitude smaller than the critical one, the non-slip condition can be satisfied.

3. Finite element modeling of tip-cantilever systems

FE methods are powerful and versatile tools for dynamic analysis of complex mechanical systems. A 3D FE beam model of tip-cantilever systems was developed by (Song and Bhushan 2006b) for simulation of the free and surface-coupled dynamics of AFM cantilevers in various dynamic modes. Representing the cantilever by 3D beam elements, this model addresses all the complexities in cantilever dynamic modeling arising from the excitation mechanism, tip geometry/location, tilting of the cantilever to the sample surface, and the couplings among the different deflections of AFM cantilevers.

3.1. Finite element beam model

The FE model of the tip-cantilever system is illustrated in figure 14. The center of the tip bottom is positioned at point A, whose coordinates are $x = \lambda L$ ($0 < \lambda \leq 1$), $y = e_t$, and $z = 0$. The distance between the mass center of the tip (point G) and point A is h_G . The cantilever is discretized by 3D beam elements, and the tip is modeled as a rigid bar. The tip-sample interaction occurring at the end of the tip (point P) is transferred to the cantilever through point C. For convenience, point C shall be a node of two adjoining beam elements.

Figure 15 shows a 3D beam element. Note that the local coordinate system of the beam elements employed

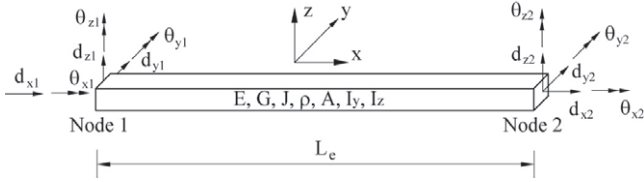


Figure 15. Three-dimensional beam element. At each node of the element, there are three translational and three rotational displacements.

to discretize the cantilever is coincident with the global coordinate system of the tip–cantilever assembly in figure 14. At each node of a 3D beam element, there are six DOFs, three translation displacements and three rotations. The element nodal displacement vector is

$$\mathbf{d}^e = \{d_{x1}, d_{y1}, d_{z1}, \theta_{x1}, \theta_{y1}, \theta_{z1}, d_{x2}, d_{y2}, d_{z2}, \theta_{x2}, \theta_{y2}, \theta_{z2}\}^T. \quad (68)$$

The corresponding element nodal force vector, consisting of three shear forces and three moments at each node, is

$$\mathbf{f}^e = \{F_{x1}, F_{y1}, F_{z1}, M_{x1}, M_{y1}, M_{z1}, F_{x2}, F_{y2}, F_{z2}, M_{x2}, M_{y2}, M_{z2}\}^T. \quad (69)$$

The element stiffness matrix expresses the relation of element nodal force vector \mathbf{f}^e with element nodal displacement vector \mathbf{d}^e . For a 3D beam element with a length of L_e , the element stiffness and mass matrices are represented by \mathbf{k}^e and \mathbf{m}^e , which are functions of geometry and material properties of the beam element. If the mass and moments of inertia of the tip are not negligible, the tip will contribute to the system mass matrix through node C. The mass matrix of the tip is represented by \mathbf{m}_t (Song and Bhushan 2006b).

The system mass and stiffness matrices \mathbf{M} and \mathbf{K} are obtained by assembling the contributions from all the beam elements and the tip. The system damping matrix \mathbf{C} is usually represented by a proportional damping matrix for simplicity (Song and Bhushan 2006a, 2006b).

The FE motion equation for the tip–cantilever system is

$$\mathbf{M}\ddot{\mathbf{d}} + \mathbf{C}\dot{\mathbf{d}} + \mathbf{K}\mathbf{d} = \mathbf{F}_{\text{ext}} + \mathbf{F}_{\text{ts}}. \quad (70)$$

Here, \mathbf{d} , $\dot{\mathbf{d}}$ and $\ddot{\mathbf{d}}$ are the system displacement, velocity and acceleration vectors, respectively, \mathbf{F}_{ext} is the force vector due to the external forces except that from the tip–sample interaction, and \mathbf{F}_{ts} is the force vector due to the tip–sample interaction. \mathbf{F}_{ts} is solely contributed by the forces and moments at node C as

$$\mathbf{F}_{\text{ts}} = \mathbf{G}_t^T \mathbf{f}_{\text{ts}}^C \quad (71)$$

where \mathbf{G}_t is the Kronecker matrix reflecting the position information of the nodal displacements at node C in the global displacement vector. As shown in figure 16, $\mathbf{f}_{\text{ts}}^C = \{f_x^C, f_y^C, f_z^C, M_x^C, M_y^C, M_z^C\}^T$ is the force vector at node C, and the vector $\mathbf{f}_{\text{ts}}^\alpha = \{f_t, f_{\text{lat}}, f_n\}^T$ contains the interaction forces on the sample surface. The transformation relation between \mathbf{f}_{ts}^C and $\mathbf{f}_{\text{ts}}^\alpha$ is given by

$$\mathbf{f}_{\text{ts}}^C = \mathbf{A}_{C\alpha} \mathbf{f}_{\text{ts}}^\alpha \quad (72)$$

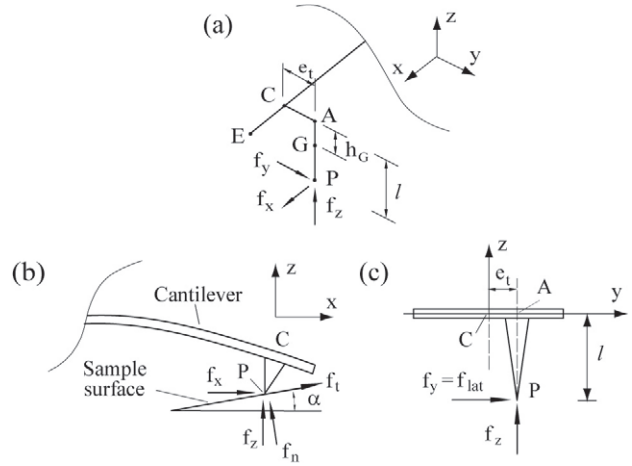


Figure 16. Force diagrams of tip–sample interaction. The cantilever is tilted to the sample surface with an angle of α and the eccentricity of the cantilever is considered. (a) 3D view. (b) View in the x – z plane. (c) View in the y – z plane.

where

$$\mathbf{A}_{C\alpha} = \begin{bmatrix} \cos \alpha & 0 & -\sin \alpha \\ 0 & 1 & 0 \\ \sin \alpha & 0 & \cos \alpha \\ e_t \sin \alpha & l & e_t \cos \alpha \\ -l \cos \alpha & 0 & l \sin \alpha \\ -e_t \cos \alpha & 0 & e_t \sin \alpha \end{bmatrix}. \quad (73)$$

If linearized tip–sample interaction is considered, one can rewrite the system motion equation (70) as

$$\mathbf{M}\ddot{\mathbf{d}} + (\mathbf{C} + \mathbf{C}_{\text{ts}})\dot{\mathbf{d}} + (\mathbf{K} + \mathbf{K}_{\text{ts}})\mathbf{d} = \mathbf{F}_{\text{ext}} + \mathbf{G}_t^T \mathbf{f}_{\text{ts}}^\alpha \quad (74)$$

where $\mathbf{f}_{\text{ts}}^\alpha$ is the force vector due to the motion of the sample surface, and \mathbf{K}_{ts} and \mathbf{C}_{ts} are the equivalent stiffness and damping contributions due to the tip–sample interaction. Equation (74) demonstrates that the linear viscoelastic tip–sample interaction is equivalent to adding additional damping and stiffness matrices to the original system.

The natural frequencies and modal shapes of the tip–cantilever system without tip–sample interaction are obtained by solving the generalized eigenvalue problems

$$\mathbf{K}\Phi = \mathbf{M}\Phi\Lambda^2 \quad (75)$$

$$\Lambda^2 = \text{diag}[\omega_1^2, \omega_2^2, \dots, \omega_n^2] \quad (76)$$

$$\Phi = [\varphi_1, \varphi_2, \dots, \varphi_n] \quad (77)$$

where n is the total number of DOFs of the system, and ω_i , φ_i and ζ_i ($i = 1, 2, \dots, n$) are the i th circular natural frequency, eigenmode vector and damping ratio of the system. The modal characteristics for a system under linear viscoelastic tip–sample interaction can be determined by solving a similar eigenvalue problem as

$$(\mathbf{K} + \mathbf{K}_{\text{ts}})\Phi_c = \mathbf{M}\Phi_c\Lambda_c^2 \quad (78)$$

$$\Phi_c = [\varphi_{c1}, \varphi_{c2}, \dots, \varphi_{cn}] \quad (79)$$

$$\Lambda_c^2 = \text{diag}[\omega_{c1}^2, \omega_{c2}^2, \dots, \omega_{cn}^2] \quad (80)$$

where ω_{ci} and φ_{ci} ($i = 1, 2, \dots, n$) are the i th circular frequency and eigenvector of the system under tip–sample interaction.

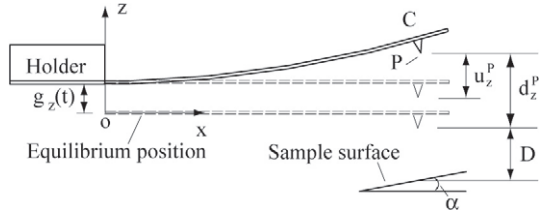


Figure 17. Schematic diagram of a cantilever in TM. The cantilever is driven to vibrate by the harmonic motion of its holder along the z axis.

3.2. Modeling of tapping mode

In TM, the cantilever is driven to vibrate by the vertical harmonic motion of its holder $g_z(t) = h_g e^{i\Omega t}$, as shown in figure 17. Except the interaction force, no external force exists ($\mathbf{F}_{\text{ext}} = \mathbf{0}$). The sample surface is fixed ($\mathbf{a}^\alpha = \mathbf{0}$). The total dynamic displacement vector of the cantilever can be expressed as

$$\mathbf{d}(t) = \mathbf{u}(t) + \mathbf{I}_z g_z(t) \quad (81)$$

where $\mathbf{u}(t)$ is the cantilever deflection relative to the moving holder. The i th element of the positioning vector \mathbf{I}_z equals unity if the i th DOF of $\mathbf{d}(t)$ corresponds to the translational displacement in the z axis; otherwise, it equals zero. The motion equation (70) can be rewritten as

$$\mathbf{M}\ddot{\mathbf{u}} + \mathbf{C}\dot{\mathbf{u}} + \mathbf{K}\mathbf{u} = -\Gamma_z \ddot{g}_z(t) + \mathbf{F}_{\text{ts}}(\mathbf{u}, \dot{\mathbf{u}}) \quad (82)$$

$$\Gamma_z = \mathbf{M}\mathbf{I}_z \quad (83)$$

when the cantilever is vibrating far away from the surface ($\mathbf{F}_{\text{ts}} = \mathbf{0}$), the vibration amplitude due to the excitation from the holder can be determined from the FRF of the system. Assuming $\mathbf{u} = \mathbf{U}e^{i\Omega t}$, one can obtain the FRF vector of the cantilever due to the z direction motion of the holder from equation (82)

$$\mathbf{H}_z(\Omega) = \frac{\mathbf{U}}{h_g} = [\mathbf{K} + i\Omega\mathbf{C} - \Omega^2\mathbf{M}]^{-1}\Gamma_z\Omega^2. \quad (84)$$

The i th element of $\mathbf{H}_z(\Omega)$, $H_{zi}(\Omega)$ ($i = 1, 2, \dots, n$), represents the response of the i th DOF of the system when the holder is moving harmonically with a unit amplitude at circular frequency Ω . If the total vertical displacement (d_z^C) and rotation about the y axis (θ_y^C) at node C are the p th and q th DOFs of the system, the free vibration amplitudes and phases of d_z^C and θ_y^C under the excitation $h_g e^{i\Omega t}$ are the amplitudes and arguments of the complex values of $[H_{zp}(\Omega) + 1]h_g$ and $H_{zq}(\Omega)h_g$, respectively. Note that the readout of the measuring system of the AFM is the signal about θ_y^C .

Under linear tip-sample interaction, the dynamic response of the tip-cantilever system can be obtained in the same way as that used in the free vibration analysis except that the system damping and stiffness matrices become $\mathbf{C} + \mathbf{C}_{\text{ts}}$ and $\mathbf{K} + \mathbf{K}_{\text{ts}}$. The surface-coupled FRF vector due to the z direction motion of the holder can be expressed as (Song and Bhushan 2006b)

$$\mathbf{H}_z^{\text{ts}}(\Omega) = \frac{\mathbf{U}}{h_g} = [(\mathbf{K} + \mathbf{K}_{\text{ts}}) + i\Omega(\mathbf{C} + \mathbf{C}_{\text{ts}}) - \Omega^2\mathbf{M}]^{-1} \times [\Gamma_z\Omega^2 - i\Omega\mathbf{C}_{\text{ts}}\mathbf{I}_z - \mathbf{K}_{\text{ts}}\mathbf{I}_z]. \quad (85)$$

With nonlinear tip-sample interaction, the motion equation (82) governs the nonlinear dynamic response of the cantilever. The temporal response of the cantilever can be solved using the Runge-Kutta algorithm. There might be couplings among the vertical bending, lateral bending, extension, and torsion of the cantilever. Equation (82) takes all the couplings, if any, into consideration. Numerical simulations have shown that in TM, compared with vertical displacement and rotation about the y axis, the displacements/rotations related to the extension, torsion, and lateral bending of the cantilever are all negligible (Song and Bhushan 2006b).

3.3. Modeling of TR and LE modes

In TR mode, the cantilever is excited by the torsional vibration of its holder $g_\theta(t) = \theta_g e^{i\Omega t}$. Except the interaction force, no external force exists ($\mathbf{F}_{\text{ext}} = \mathbf{0}$). The sample surface is fixed ($\mathbf{a}^\alpha = \mathbf{0}$). The total dynamic displacement vector of the cantilever can be expressed as

$$\mathbf{d}(t) = \mathbf{u}(t) + \mathbf{I}_\theta g_\theta(t) \quad (86)$$

where $\mathbf{u}(t)$ is the cantilever deflection relative to the rotating holder, and $g_\theta(t)$ is the torsional motion of the holder. The i th element of the positioning vector \mathbf{I}_θ equals unity if the i th DOF of $\mathbf{d}(t)$ corresponds to the torsion about the x axis; otherwise, it equals zero. The motion equation is

$$\mathbf{M}\ddot{\mathbf{u}} + \mathbf{C}\dot{\mathbf{u}} + \mathbf{K}\mathbf{u} = -\Gamma_\theta \ddot{g}_\theta(t) + \mathbf{F}_{\text{ts}}(\mathbf{u}, \dot{\mathbf{u}}) \quad (87)$$

$$\Gamma_\theta = \mathbf{M}\mathbf{I}_\theta. \quad (88)$$

In free vibration ($\mathbf{F}_{\text{ts}} = \mathbf{0}$), the FRF vector due to the torsion of the holder is Song and Bhushan (2006b)

$$\mathbf{H}_\theta(\Omega) = \frac{\mathbf{U}}{\theta_g} = [\mathbf{K} + i\Omega\mathbf{C} - \Omega^2\mathbf{M}]^{-1}\Gamma_\theta\Omega^2. \quad (89)$$

If θ_x^C is the m th DOF of the system, the total free vibration amplitude and phase of θ_x^C under a harmonic motion of the holder $g_\theta(t) = \theta_g e^{i\Omega t}$ are the amplitude and argument of the complex value of $[H_{\theta m}(\Omega) + 1]\theta_g$, respectively.

If the tip-sample separation (normal pressure) remains almost constant during measurement, the tip-sample interaction can be modeled using a linear viscoelastic model. The FRF vector due to the torsion of the holder under tip-sample interaction is (Song and Bhushan 2006b)

$$\mathbf{H}_\theta^{\text{ts}}(\Omega) = \frac{\mathbf{U}}{\theta_g} = [(\mathbf{K} + \mathbf{K}_{\text{ts}}) + i\Omega(\mathbf{C} + \mathbf{C}_{\text{ts}}) - \Omega^2\mathbf{M}]^{-1} \times [\Gamma_\theta\Omega^2 - i\Omega\mathbf{C}_{\text{ts}}\mathbf{I}_\theta - \mathbf{K}_{\text{ts}}\mathbf{I}_\theta]. \quad (90)$$

The temporal response of the cantilever can be obtained by solving the motion equation (87) using the Runge-Kutta algorithm. The deflection of the cantilever in TR mode is a combination of torsion and lateral bending. If tip eccentricity exists ($e_t \neq 0$), the twist of the cantilever will change the tip-sample distance and consequently the normal interaction force. In this case, the vertical bending and extension will be coupled with the torsion/lateral bending of the cantilever. However, in TR mode, the deflections of the cantilever corresponding to the

vertical bending and extension are small and can be ignored (Song and Bhushan 2006b).

In LE mode, the cantilever is excited to vibrate by the harmonic motion of the sample surface ($\mathbf{a}^\alpha \neq \mathbf{0}$) through the lateral tip-sample interaction. The driving frequency could be a value in a wide range around the resonance frequencies of torsion or lateral bending. Except the interaction force, no external force exists ($\mathbf{F}_{\text{ext}} = \mathbf{0}$). The system motion equation of the LE mode is

$$\mathbf{M}\ddot{\mathbf{d}} + \mathbf{C}\dot{\mathbf{d}} + \mathbf{K}\mathbf{d} = \mathbf{F}_{\text{ts}}(\mathbf{d}, \dot{\mathbf{d}}). \quad (91)$$

The motion of the sample surface is

$$\mathbf{a}^\alpha = \{a_t, a_{\text{lat}}, a_n\}^T = \{0, a_g e^{i\Omega t}, 0\}^T. \quad (92)$$

If the tip-sample separation (normal pressure) remains almost constant during the measurement, tip-sample interaction can be modeled using a linear viscoelastic model. The motion equation of (91) can then be expressed as

$$\mathbf{M}\ddot{\mathbf{d}} + (\mathbf{C} + \mathbf{C}_{\text{ts}})\dot{\mathbf{d}} + (\mathbf{K} + \mathbf{K}_{\text{ts}})\mathbf{d} = \mathbf{G}_{\text{t}}^T \mathbf{f}_{\text{ts}}^a \quad (93)$$

$$\mathbf{f}_{\text{ts}}^a = \mathbf{A}_{\text{C}\alpha} (\mathbf{k}_{\text{ts}}^\alpha \mathbf{a}^\alpha + \mathbf{c}_{\text{ts}}^\alpha \dot{\mathbf{a}}^\alpha) \quad (94)$$

$$\mathbf{k}_{\text{ts}}^\alpha = \begin{bmatrix} k_t & 0 & 0 \\ 0 & k_{\text{lat}} & 0 \\ 0 & 0 & k_n \end{bmatrix}, \quad \mathbf{c}_{\text{ts}}^\alpha = \begin{bmatrix} c_t & 0 & 0 \\ 0 & c_{\text{lat}} & 0 \\ 0 & 0 & c_n \end{bmatrix}. \quad (95)$$

By substituting equations (92) and (94) into (93) and assuming $\mathbf{d} = \mathbf{U}e^{i\Omega t}$, one can rewrite the motion equation as

$$[-\Omega^2 \mathbf{M} + i\Omega(\mathbf{C} + \mathbf{C}_{\text{ts}}) + (\mathbf{K} + \mathbf{K}_{\text{ts}})]\mathbf{U} = \Gamma_{\text{lat}} a_g \quad (96)$$

$$\begin{aligned} \Gamma_{\text{lat}} &= \mathbf{G}_{\text{t}}^T \mathbf{A}_{\text{C}\alpha} \left(\mathbf{k}_{\text{ts}}^\alpha \begin{Bmatrix} 0 \\ 1 \\ 0 \end{Bmatrix} + \mathbf{c}_{\text{ts}}^\alpha \begin{Bmatrix} 0 \\ i\Omega \\ 0 \end{Bmatrix} \right) \\ &= \mathbf{G}_{\text{t}}^T \begin{Bmatrix} 0 \\ k_{\text{lat}} + i\Omega c_{\text{lat}} \\ 0 \\ l(k_{\text{lat}} + i\Omega c_{\text{lat}}) \\ 0 \\ 0 \end{Bmatrix}. \end{aligned} \quad (97)$$

The FRF vector due to the motion of the sample in LE mode is (Song and Bhushan 2006b)

$$\mathbf{H}_{\text{lat}}(\Omega) = \frac{\mathbf{U}}{a_g} = [(\mathbf{K} + \mathbf{K}_{\text{ts}}) + i\Omega(\mathbf{C} + \mathbf{C}_{\text{ts}}) - \Omega^2 \mathbf{M}]^{-1} \Gamma_{\text{lat}}. \quad (98)$$

The readout of the AFM measuring system is the signal about θ_x^C . If θ_x^C is the m th DOF of the system, the total free vibration amplitude and phase of θ_x^C under a harmonic motion of the holder $a_{\text{lat}}(t) = a_g e^{i\Omega t}$ are the amplitude and argument of the complex value of $H_{\text{lat } m}(\Omega) a_g$, respectively.

The coupling relations in LE mode are the same as these in TR mode. The response of the cantilever, equation (93), can be solved using the Runge-Kutta algorithm.

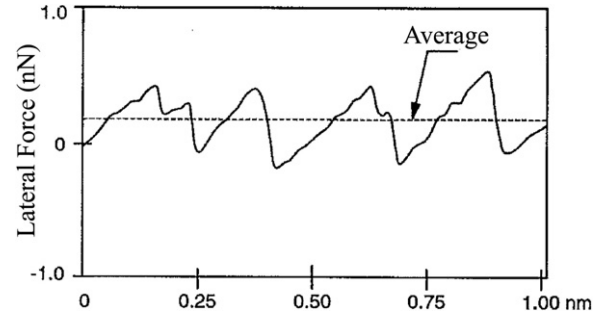


Figure 18. Stick-slip tip motion obtained in atomic-scale friction measurement. The experiment was conducted on a freshly cleaved HOPG sample using a silicon nitride cantilever with a sharp tip (Ruan and Bhushan 1994).

4. Applications of FE model in AFM mode simulations

4.1. FFM profiling process simulation

FFM is usually categorized as one of the static AFM modes because during measurement the cantilever is not excited to vibrate, and under certain conditions the cantilever is indeed in the quasi-static motion. Nevertheless, stick-slip tip motion is often observed in friction measurement, as shown in figure 18 (Ruan and Bhushan 1994). In that case, cantilever dynamics is closely correlated to the measured topographic and friction images and has to be considered.

4.1.1. Cantilever deflection in FFM. The working mechanism of an optical beam-deflection FFM can be explained in figure 1. FFM allows simultaneous measurements of surface topography, normal and lateral forces. The four-segment photo-diode is used to measure the cantilever flexural angle θ_y^C and twist angle θ_x^C . Refer to figure 16; with tip eccentricity and the tilting of the cantilever to the sample surface being neglected, the vertical bending is solely caused by the normal force f_z and the moment $M_y^C = -f_x l$ resulting from the lateral force f_x . The lateral force f_y causes the lateral bending, and its resulting torque $f_y l$ twists the cantilever. Extension occurs due to the lateral force f_x , but usually it is very small and thus can be neglected. For a typical cantilever, the extension stiffness is four to five orders of magnitude higher than that of vertical bending.

θ_y^C is the flexural angle of the cantilever due to vertical bending. It is related to the normal load f_z and lateral force f_x . However, the contribution from f_x to θ_y^C is much smaller than that from f_z , and therefore, normal load f_z can be viewed as the sole cause of θ_y^C (Song and Bhushan 2006d). With the help of a feedback loop in FFM, surface topography (or constant normal force profile) can be obtained by keeping a constant θ_y^C through the z -direction motion of the piezotube when the cantilever tip is scanned over the sample surface. Since the lateral force f_y is the only interaction force that is responsible for the cantilever torsion, the twist angle θ_x^C is a good measurement for f_y .

In the constant-force mode of FFM, a constant normal load (or, equivalently, a constant θ_y^C) is maintained to make

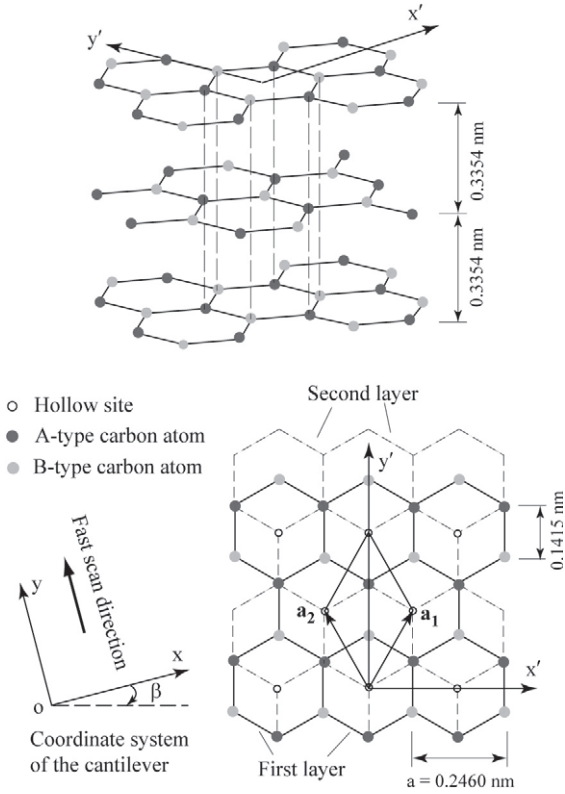


Figure 19. Schematic view of the periodic hexagonal lattice structure of (0001) graphite surface. Layers of the hexagonal structures are staggered with a distance of 0.3354 nm. Two types of atoms are distinguished. Hollow sites are the centers of each hexagon. In the coordinate system for the cantilever, the x axis is along the cantilever longitudinal direction. The cantilever is always scanned along the y axis in constant-force mode of FFM. Another coordinate system (x' , y') is introduced for convenient determination of atom locations on the graphite surface. The shown parallelogram is a primitive unit cell which includes two carbon atoms. Vectors \mathbf{a}_1 and \mathbf{a}_2 are the unit lattice vectors for the primitive unit cell. The angle β is defined to represent the relation between the coordinate systems for the cantilever and graphite lattice structure.

the measured results meaningful. During the measurement, the (fast) scan direction is perpendicular to the longitudinal direction of the cantilever (along the y axis), and the lateral force f_y is obtained by measuring the twist angle θ_x^C . During measurement, the tip is always in a stable equilibrium state in the vertical direction if the holder is moving with a moderate scan speed. In this case, the vertical displacement and flexural angle can be obtained by

$$d_z^C = \text{constant} = \frac{L^3}{3EI_y} f_z + \frac{L^2 l}{2EI_y} f_x \quad (99)$$

$$\theta_y^C = \text{constant} = -\frac{L^2}{2EI_y} f_z - \frac{Ll}{EI_y} f_x. \quad (100)$$

With the contribution of f_x being neglected, we have $d_z^C \approx \frac{L^3}{3EI_y} f_z$ and $\theta_y^C \approx -\frac{L^2}{2EI_y} f_z$. Therefore, the topography map obtained in FFM, $z_t(x_t, y_t)$, can be obtained by solving the nonlinear equation

$$f_z(x_t, y_t, z_t) = W \quad (101)$$

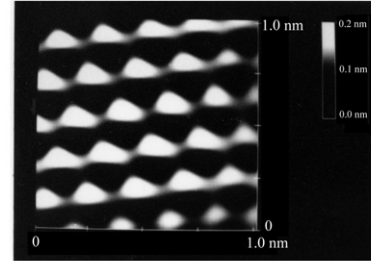
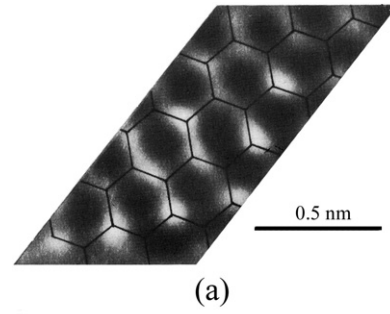


Figure 20. AFM topography images of graphite surface. (a) Topography image of graphite obtained with a cantilever without a tip (Binnig *et al* 1987). Hexagonal structure of the graphite surface is shown. (b) Topography map of HOPG showing atomic resolution of every other atom (Ruan and Bhushan 1994).

where (x_t, y_t, z_t) are coordinates of the cantilever tip and W is the applied normal load.

4.1.2. FFM images of graphite surface. Atomic-scale topographic imaging has been carried out by researchers on HOPG and other samples. Figure 19 shows the hexagonal structure of a (0001) graphite surface. Layers of the hexagonal structures are staggered with a distance of 0.3354 nm. Two types of carbon atoms, A type and B type, exist due to the way the layers are staggered. A-type atoms have a direct neighbor in the adjacent layers while B-type atoms do not. Within one layer, the distance between the adjacent A-type or B-type atoms is 0.2460 nm, and it is 0.1415 nm between any two adjacent carbon atoms. Binnig *et al* (1987) successfully observed the hexagonal structure of a graphite surface (see figure 20(a)). In their experiment, a cantilever without a tip was scanned over the graphite surface with its corner touching the surface to obtain the topographic images. Marti *et al* (1987) also obtained the full hexagonal topographic image of a graphite surface covered with paraffin oil using a diamond epoxied to one of the four cross-points of four platinum wires. However, many others (Albrecht and Quate 1987, Ruan and Bhushan 1994) could only show the trigonal lattice of three peaks with a distance of about 0.246 nm in their experimentally obtained topographic images, i.e., so called ‘atomic resolution of every other atom’ (see figure 20(b)).

FFM topographic and friction images are closely correlated to the cantilever dynamics. The friction force map measured in FFM is actually the map about the cantilever torsional angle θ_x^C and the topographic map is about the z -direction holder motion z_h . In the measured maps of FFM,

the topography and lateral forces at the locations of the tip $(x_t(t), y_t(t))$ are plotted against the ‘nominal’ coordinates of the tip, i.e. the tip position at time t if the cantilever is rigid (no deflection). The ‘nominal’ tip coordinates are determined from the coordinate of the cantilever holder. Here, we represent them as $(x_h(t) + L_h, y_h(t))$, where $(x_h(t), y_h(t))$ are coordinates of the holder and L_h is a constant in each experiment. Due to the cantilever deflection during measurements, usually one will find that the ‘nominal’ tip coordinates $(x_h(t) + L_h, y_h(t))$ are different from the real tip coordinates $(x_t(t), y_t(t))$. This means that cantilever dynamics have to be considered in order to explain the aforementioned different experimentally obtained topography of graphite.

4.1.3. Modeling of FFM profiling process. The interaction forces between the scanning cantilever tip and the graphite surface can be calculated from the spatial derivatives of an interaction potential between the atoms of the tip and graphite surface. The periodic structure of the graphite surface induces a periodic interaction potential in the form of

$$V_{ts}(\mathbf{r}_t) = V_{ts}(\mathbf{r}_t + i_1 \mathbf{a}_1 + i_2 \mathbf{a}_2) \quad (102)$$

where \mathbf{r}_t is the tip position vector, \mathbf{a}_1 and \mathbf{a}_2 are the unit lattice vectors in the surface plane (refer to figure 19), and i_1 and i_2 are arbitrary integers. It is assumed that the interaction potential between the tip and graphite surface equals the sum of the interaction potential between individual tip atoms and carbon atoms of the graphite surface. In the (x, y, z) coordinate system of the cantilever, the tip position vector is denoted as $\mathbf{r}_t = (x_t, y_t, z_t)$.

Using the 3D finite element beam model described in section 3, the motion equation governing the cantilever response is expressed as

$$\mathbf{M}\ddot{\mathbf{u}} + \mathbf{C}\dot{\mathbf{u}} + \mathbf{K}\mathbf{u} = \mathbf{F}_{ts} - \mathbf{M}\Gamma\ddot{\mathbf{g}}_h. \quad (103)$$

Here, \mathbf{u} , $\dot{\mathbf{u}}$ and $\ddot{\mathbf{u}}$ are displacement, velocity and acceleration vectors of the cantilever relative to its holder, $\mathbf{g}_h = \{x_h, y_h, z_h\}^T$ is the vector of holder motion, and Γ is the position matrix to describe the relation between the total displacement vector \mathbf{u}_{tot} and \mathbf{u} . The total displacement vector of the cantilever in the (x, y, z) coordinate system is expressed as

$$\mathbf{u}_{\text{tot}} = \mathbf{u} + \Gamma \mathbf{g}_h. \quad (104)$$

For easy illustration, it is assumed that the tip is at the end of the cantilever, and the cantilever is represented by only one beam element. There are six DOFs at the end of the cantilever: $d_x^C, d_y^C, d_z^C, \theta_x^C, \theta_y^C$, and θ_z^C . The extension of the cantilever can be neglected, i.e., $d_x^C = 0$.

The cantilever deflections corresponding to lateral bending (d_y^C and θ_z^C) and torsion (θ_x^C) are governed by equation (103). The cantilever is scanned with a constant velocity, i.e., $\ddot{\mathbf{g}}_h = \{0, 0, 0\}^T$. Equation (103) is expressed as

$$\begin{aligned} & \rho A L \begin{bmatrix} 39/105 & 0 & -11L/210 \\ 0 & I_p/3A & 0 \\ -11L/210 & 0 & L^2/105 \end{bmatrix} \begin{Bmatrix} \ddot{d}_y^C \\ \ddot{\theta}_x^C \\ \ddot{\theta}_z^C \end{Bmatrix} \\ & + \begin{bmatrix} c_{11} & c_{12} & c_{13} \\ c_{21} & c_{22} & c_{23} \\ c_{31} & c_{32} & c_{33} \end{bmatrix} \begin{Bmatrix} \dot{d}_y^C \\ \dot{\theta}_x^C \\ \dot{\theta}_z^C \end{Bmatrix} \\ & + \begin{bmatrix} 12EI_z/L^3 & 0 & -6EI_z/L^2 \\ 0 & GJ/L & 0 \\ -6EI_z/L^2 & 0 & 4EI_z/L \end{bmatrix} \begin{Bmatrix} d_y^C \\ \theta_x^C \\ \theta_z^C \end{Bmatrix} \\ & = \begin{Bmatrix} f_y^C \\ M_x^C \\ M_z^C \end{Bmatrix}. \end{aligned} \quad (105)$$

The force and moment at point C are related to f_y as

$$\begin{Bmatrix} f_y^C \\ M_x^C \\ M_z^C \end{Bmatrix} = \begin{Bmatrix} 1 \\ l \\ 0 \end{Bmatrix} f_y(x_t, y_t, z_t). \quad (106)$$

The lateral force f_y is a function of the tip location, which can be determined from the constant-force condition in equation (101) and the cantilever deflection as follows:

$$x_t = x_h + L - l\theta_y^C, \quad y_t = y_h + d_y^C + l\theta_x^C. \quad (107)$$

In equation (107), $-l\theta_y^C \approx \frac{L^2 l}{2EI_y} f_z = \text{constant}$, i.e., along each scan line $x_t = \text{constant}$. Equation (105) is nonlinear and needs to be solved numerically with equation (101) to simulate the cantilever response in FFM. The resulting maps of z_t and θ_x^C are the FFM imaging results of topographic and friction force, respectively.

The damping matrix in equation (105) addresses the energy dissipation mechanism in the tip–cantilever–surface system. It includes both the material damping in the cantilever and the energy dissipation induced from the tip–sample interaction, such as phonon generation. It is demonstrated in section 3 that the damping effects due to the tip–sample interaction can be equivalently addressed as an additional damping term to the material damping matrix of the cantilever. Here, the damping matrix is calculated as

$$\mathbf{C} = [\boldsymbol{\varphi}_1, \boldsymbol{\varphi}_2, \boldsymbol{\varphi}_3]^{-T} \text{diag}(2\zeta_1\omega_1, 2\zeta_2\omega_2, 2\zeta_3\omega_3) [\boldsymbol{\varphi}_1, \boldsymbol{\varphi}_2, \boldsymbol{\varphi}_3]^{-1} \quad (108)$$

where ω_i , $\boldsymbol{\varphi}_i$ and ζ_i ($i = 1, 2, 3$) are the i th circular natural frequency, normalized eigenmode vector and damping ratio of the system. Large damping ratios (close to 1.0) are adopted to simulate the damping effects in the profiling process of FFM.

4.1.4. Simulations on graphite surface. The FFM profiling process was simulated by Song and Bhushan (2006d) for different combinations of normal loads, tip lengths, and scan directions. Figure 21 shows the simulated maps of cantilever twist angle $-\theta_x^C$, the tip-distance map z_t , and the paths of the cantilever tip. The maps of $-\theta_x^C$ can be viewed as a measurement of the lateral force that resists the movement of the cantilever, i.e., the lateral force whose direction is opposite

to the scan direction. The rectangular silicon cantilever considered here has the following dimensional and material parameters: $L = 252 \mu\text{m}$, $b = 35 \mu\text{m}$, $h = 2.3 \mu\text{m}$, $\rho = 2330 \text{ kg m}^{-3}$, $E = 1.3 \times 10^{11} \text{ Pa}$, $\nu = 0.28$.

A. Slow-fast motion pattern. In figure 21(a), the results are for the normal load $W = 10 \text{ nN}$, tip length $l = 12.5 \mu\text{m}$, and $\beta = 0^\circ$. The full hexagonal structure of the graphite surface can be seen in the topographic map. The paths of the cantilever tip are plotted by dots separated by equal time intervals. Although the cantilever holder moves with a constant velocity, the cantilever tip does not slide over the surface smoothly. The dense part on the tip paths indicates that the tip is moving slowly over the surface while the sparse part represents a faster motion. This ‘slow-fast’ motion of the cantilever tip is slightly different from what is well known as the ‘stick-slip’ behavior since ‘stick’ means that there is absolutely no relative motion between the cantilever tip and sample surface. However, as the dense and sparse parts become remarkable, the ‘slow-fast’ motion pattern is referred to as ‘stick-slip.’ Figure 21(b) gives the results under the same conditions as those in figure 21(a), except that the normal load is increased from 10 to 25 nN. The slow-fast tip motion in figure 21(b) is more remarkable than that in figure 21(a) due to the increased normal load. Consequently, the hexagonal structure in topography cannot be observed in figure 21(b) and only the ‘resolution of every other atom’ is shown. Also, a dramatic difference can be seen in the lateral force maps in figures 21(a) and (b).

B. Conditions for stick-slip occurrence. One would ask under what circumstances the stick-slip (or remarkable slow-fast) tip motion will not occur so that the detection of the full atomic structure becomes possible. It is generally recognized that stick-slip will occur if a soft cantilever is scanned over a surface with large lateral forces (Mate *et al* 1987, Sasaki *et al* 1996, Hölscher *et al* 1997). Experimentally, it is also observed that the sticking domain decreased with decreasing normal load, and under lower normal load the tip shows smoother motion (Fujisawa *et al* 1998). Johnson and Woodhouse (1998) assumed a sinusoidal lateral force and gave the analytical condition under which the tip motion is steady and no stick-slip occurs,

$$T^* < T_c^* = \lambda_1 c_e / 2\pi \quad (109)$$

where T^* is the magnitude of the sinusoidal lateral force, T_c^* is the critical lateral force magnitude at which stick-slip will occur, λ_1 is the periodic lattice spacing of the sample surface, and c_e is the effective lateral stiffness. Although equation (109) is obtained under the assumption of a sinusoidal lateral force, it may be used for a rough estimation of the occurrence of stick-slip in the simulations. For a rigid surface, c_e equals the static lateral stiffness of the cantilever, i.e.,

$$c_e = \left(\frac{L^3}{3EI_z} + \frac{Ll^2}{GJ} \right)^{-1}. \quad (110)$$

For the cantilever in figures 21(a) and (b), $c_e = 94.4 \text{ N m}^{-1}$. If it is chosen as $\lambda_1 = 0.426 \text{ nm}$, the critical lateral force

Table 5. Conditions for stick-slip occurrence.

	Applied load	Cantilever lateral stiffness	Cantilever geometry
Stick-slip	Large	Small	Smaller width, smaller thickness, larger length, larger tip length
No stick-slip	Small	Large	Larger width, larger thickness, smaller length, smaller tip length

magnitude is $T_c^* = 6.4 \text{ nN}$. The maximum lateral force is about 3 nN for $W = 10.0 \text{ nN}$ and about 10 nN for $W = 25.0 \text{ nN}$. According to the condition in equation (110), stick-slip should happen in figure 21(b) but not in figure 21(a), which is consistent with the simulated results.

C. Methods for stick-slip prevention. To observe the full atomic structure of the surface, the velocity of the cantilever tip should not oscillate too much during the scanning process. As pointed out earlier, this usually requires a relatively small lateral force and a large lateral stiffness of the cantilever. With the same normal load as that in figure 21(b), figure 21(c) shows the results with a smaller tip length $l = 2.5 \mu\text{m}$. As expected, the slow-fast tip motion in figure 21(c) becomes less remarkable than that in figure 21(b), and the full hexagonal lattice structure is shown in the topographic map although the normal load is the same as that in figure 21(b). With a tip length of $2.5 \mu\text{m}$, $c_e = 194.1 \text{ N m}^{-1}$, and the critical lateral force magnitude $T_c^* = 13.2 \text{ nN}$. According to equation (109), the stick-slip motion should not occur. Actually, this was exactly what Binnig *et al* (1987) did in their experiment where the full atomic structure was obtained successfully. In their experiment, a cantilever without a tip was used. During measurement, the cantilever corner touched the sample surface for imaging. In the other experiment by Marti *et al* (1987), in which the full hexagonal structure of graphite surface was observed, a totally different detecting-sensing design was employed. The lateral stiffness of the wires they used is about $8 \times 10^4 \text{ N m}^{-1}$, which is much stiffer than the commercially available cantilevers, whose lateral stiffness is typically $10\text{--}500 \text{ N m}^{-1}$. Table 5 summarizes the conditions for stick-slip occurrence.

D. Image patterns due to different scan directions. In figure 21(d), the results are for the normal load $W = 25 \text{ nN}$, tip length $l = 12.5 \mu\text{m}$, and $\beta = 30^\circ$. Compared with figure 21(b), the effects of scan direction on topographic and lateral force maps can be seen. Different patterns of tip paths are also shown. The differences of figures 21(b) and (d) can be explained by the different distributions of atom locations. The peaks of topography for $\beta = 0^\circ$ appear at the place where the tip is scanned between two closely placed atoms (Song and Bhushan 2006d). When $\beta = 30^\circ$, two different areas can be distinguished. In area A, there is no carbon atom in the way of the scanned tip, resulting in a stripe-like dark area.

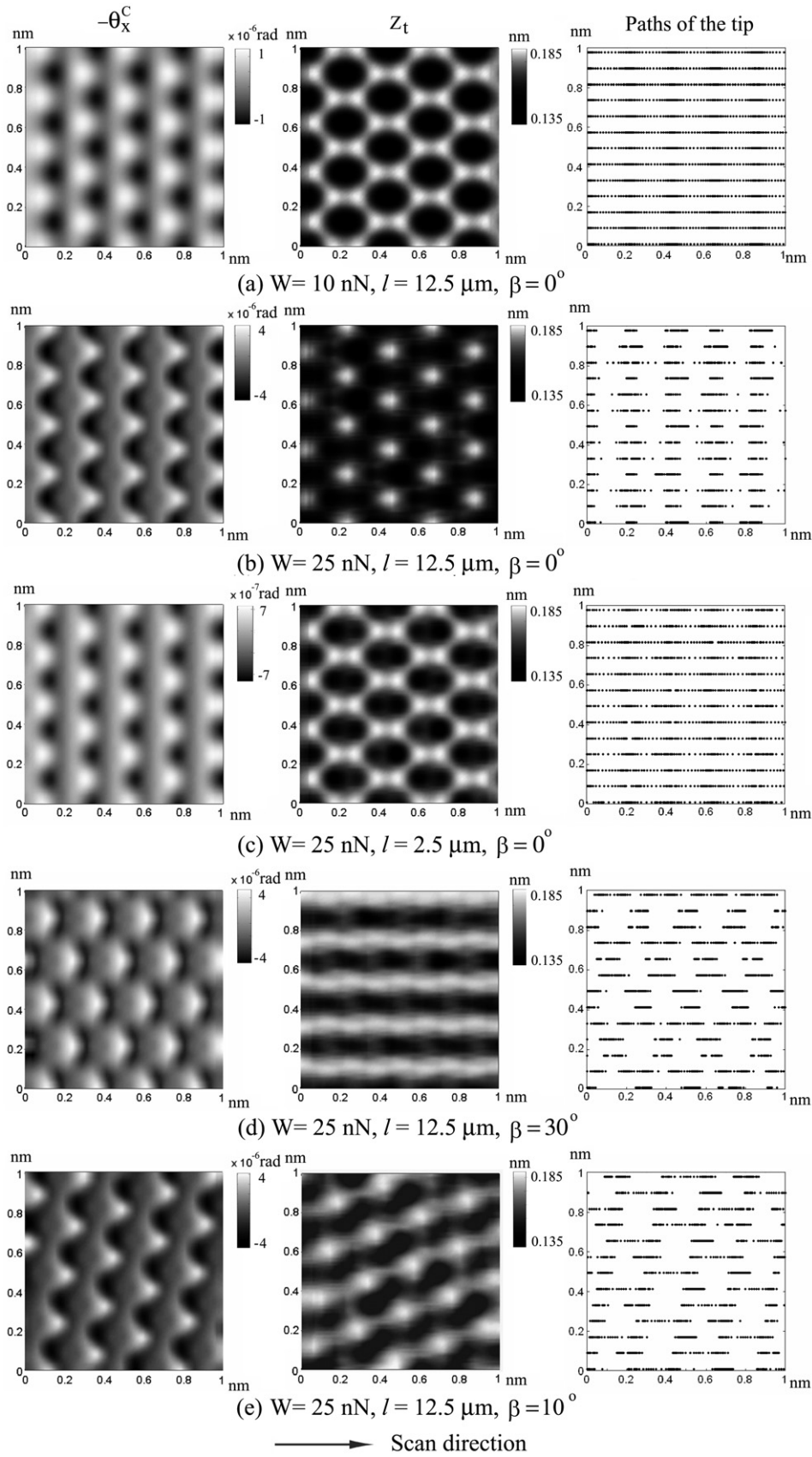


Figure 21. The simulated maps of cantilever twist angle $-\theta_x^C$ (left-hand column), tip-surface distance (middle column) z_t , and 13 paths of the cantilever tip (right-hand column) for different combinations of the normal loads, tip lengths, and scan directions. The maps of cantilever twist angle are equivalent to the lateral force maps. The tip-surface distance maps are equivalent to the topographic maps. The data on the maps are unit-cell averaged. The paths of the tip is ‘time resolved’, i.e., the paths are plotted by dots separated by equal time intervals $\Delta t = 0.05 \text{ ms}$.

Table 6. Relations of scan direction and characteristics of topographic maps of graphite, when stick-slip tip motion occurs or does not occur.

	Scan angle β		
	Close to 0° (or 60°)	Close to 30°	Between 0° and 30° , or between 30° and 60°
Stick-slip	Trigonal structure	Stripe-like structure	Between trigonal and stripe-like structure
No stick-slip	Hexagonal structure	Hexagonal structure	Hexagonal structure

Area B is the narrow stripe where the atoms are located. Due to the unsmooth motion of the tip, the topography in this area is ‘averaged’ and thus a stripe-like bright area is shown.

Figure 21(e) shows the results for the normal load $W = 25$ nN, tip length $l = 12.5$ μm , and $\beta = 10^\circ$. The simulated topographic map is very similar to some of the scanning tunneling microscopy (STM) experimental results (Mizes *et al* 1987). Compared with figures 21(b) (trigonal topography) and 21(d) (stripe-like topography), figure 21(e) can be viewed as something between the two. The scan directions of $\beta = 0^\circ$ and 30° are two extreme cases regarding the atom location distribution. Any scan direction in the range of $(0^\circ, 30^\circ)$ and $(30^\circ, 60^\circ)$ should result in lateral force and topography images that are something between the results for $\beta = 0^\circ$ and 30° . The closer β is to 0° or 60° , the more the images are similar to those in figure 21(b). While β is close to 30° , the resulting images should look more like those shown in figure 21(d). Table 6 summarizes the relations of scan direction and characteristics of topographic maps of graphite, when stick-slip tip motion occurs or does not occur.

4.2. Vibration analysis of AFM tapping mode in liquid

Investigation of morphology and mechanical properties of biological specimens using AFM often requires its operation in a liquid environment. Due to hydrodynamic force, the vibration of AFM cantilevers in liquid shows dramatically different dynamic characteristics from that in air. A good understanding of the dynamics of AFM cantilevers vibrating in liquid is needed for interpretation of scanning images and selection of AFM operating conditions.

4.2.1. Experiment measurement. In biology, operating AFM in liquid allows the investigation of morphology and mechanical properties of biological samples in their native solutions. Other advantages include the elimination of capillary forces (Drake *et al* 1989), reduction of van der Waals forces by tenfold or more (Goodman and Garcia 1991), and reduced tip and sample contamination (Hansma *et al* 1994). Pioneering images of biological samples in liquid were acquired using contact mode AFM (Drake *et al* 1989, Hansma *et al* 1992). In contact mode AFM, the cantilever tip is in constant contact with the surface, and the resulting lateral force could be destructive to soft samples. TM in liquid was first implemented by Putman *et al* (1994). They successfully measured the frequency responses and tip-sample approach

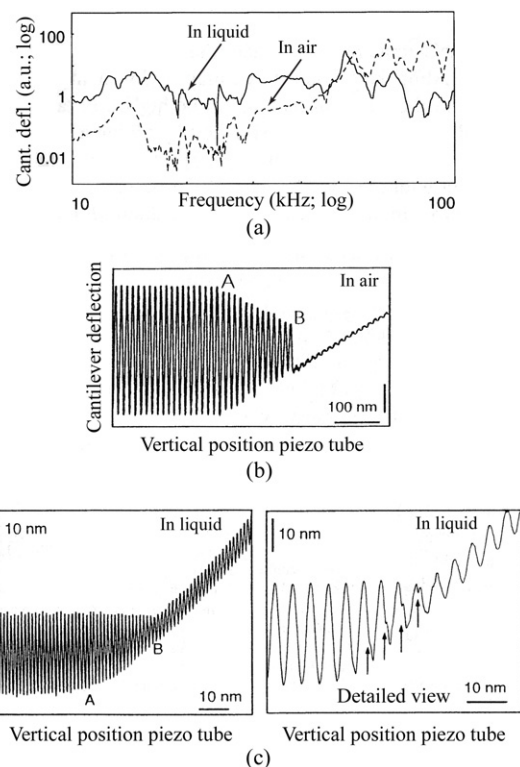


Figure 22. Experimental measurements of AFM cantilever responses in air and liquid (Putman *et al* 1994). (a) Amplitude of cantilever vertical displacement as a function of the driving frequency in air and liquid. (b) Cantilever vertical displacement as a function of tip-sample separation in air while the cantilever is driven to oscillate at 52 kHz. (c) Cantilever vertical displacement as a function of tip-sample separation in liquid while the cantilever is driven to oscillate at 14.1 kHz. The figures on the left and right are the same but demonstrated in different scales. The cantilever vertical displacements here were calibrated from the cantilever rotation angles measured by the AFM detecting system (Song and Bhushan 2007).

curves of V-shaped silicon nitride cantilevers in both air and liquid. It is worthwhile to mention that Hansma *et al* (1994) also made ‘tapping mode’ measurements on biological samples in liquid with a different design. In their implementation, it is the sample surface that oscillates up and down to tap the cantilever tip.

The TM frequency responses and tip-sample approach curves in both air and liquid obtained by Putman *et al* (1994) are shown in figure 22. Figure 22(a) shows the cantilever vibration amplitudes as functions of driving frequency. Due to the additional mass and damping exerted on the cantilever from the surrounding liquid, the resonances are shifted to the left, and the vibration amplitudes are quenched.

Figures 22(b) and (c) give the cantilever vertical displacements as functions of tip-sample separation in air and liquid, respectively. During the measurements, the cantilever was under constant vibrational excitation near resonance frequencies, and it was brought towards the sample surface with a constant velocity. In air (figure 22(b)), three regimes can be observed in the cantilever response. Left to point A, the cantilever oscillates away from the sample surface

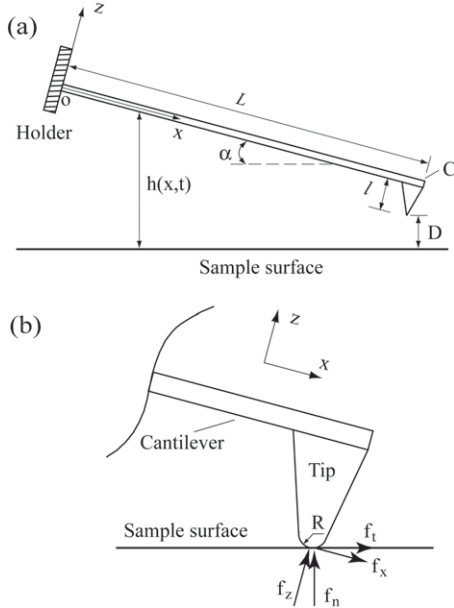


Figure 23. Schematic diagrams of a tip–cantilever system tilted to the sample surface with an angle of α (a), and tip–sample interaction (b) (Song and Bhushan 2007).

with a constant amplitude. From point A, the cantilever tip begins to tap the surface. Between points A and B, the vibration amplitude decreases linearly as the cantilever approaches towards the surface. Beyond point B, the tip does not have sufficient energy to overcome the adhesion force and is continuously in contact with the surface.

In liquid (figure 22(c)), before the tip touches the surface, the cantilever vibrates at a constant amplitude. After a tap occurs at point A, the cantilever response shows different characteristics than that in air. Between points A and B, the bottom envelope of the cantilever oscillation decreases as the cantilever approaches the surface but the upper envelope of the oscillation hardly changes, showing an unsymmetric amplitude change in the tapping region. In addition, the bottom envelope of the oscillation does not change linearly. From point B on, the tip is permanently in contact with the sample surface. The cantilever is actually rotating with the tip as the pivot point on the surface. The rotation angle (about the y axis) oscillates with a constant amplitude but its mean shifts upwards with the same velocity as that of the cantilever approaching the surface. The right figure in figure 22(c) demonstrates the transition from free cantilever movement to the pivoting movement during the permanent contact. We note that in AFM cantilever vertical displacements are calculated by calibrating the measured rotation angles of the cantilever. This is why in figure 22(c), although the cantilever tip is actually stuck on the surface, it seems that the cantilever still has an oscillating vertical deflection.

4.2.2. Tapping mode modeling in liquid. Modeling of cantilever vibration in TM operated in liquid is a more difficult task than that in air. In a liquid environment, the cantilever behavior is dominated by the large hydrodynamic

damping and the additional mass from the liquid. Chen *et al* (1995, 1996) studied the frequency and transient responses of AFM cantilevers immersed in liquid by representing the cantilevers as spheres oscillating in viscous liquid. Also using a point-mass model, Burnham *et al* (1997) obtained the tip–sample approach curves. Their results in air agree well with the experimental ones. Sader (1998) gave a general theoretical model for frequency response analysis of a cantilever immersed in viscous liquid. This model is valid for beams vibrating with small amplitudes and whose lengths are much larger than their widths. Rankl *et al* (2004) studied the frequency response of AFM cantilevers close to the sample surface. In their model, the hydrodynamic damping due to the fluid squeezed in and out of the region between the cantilever and sample surface is considered.

Song and Bhushan (2007) used the FE beam model introduced in section 3 to simulate cantilever dynamics in TM operated in liquid. The FE motion equation of a cantilever operated in tapping mode and immersed in liquid is

$$\mathbf{M}\ddot{\mathbf{u}} + \mathbf{C}\dot{\mathbf{u}} + \mathbf{K}\mathbf{u} = \mathbf{F}_{ts} - \mathbf{M}\mathbf{I}_z\ddot{g}_z(t) - \mathbf{F}_d. \quad (111)$$

Compared with the cantilever motion equation in air (equation (82)), equation (111) includes a hydrodynamic force vector \mathbf{F}_d . The additional force vector \mathbf{F}_d can be approximately expressed as

$$\mathbf{F}_d = -\mathbf{M}_a\ddot{\mathbf{d}} - \mathbf{C}_a\dot{\mathbf{d}} = -\mathbf{M}_a[\ddot{\mathbf{u}} + \mathbf{I}_z\ddot{g}_z(t)] - \mathbf{C}_a[\dot{\mathbf{u}} + \mathbf{I}_z\dot{g}_z(t)]. \quad (112)$$

Then equation (111) can be rewritten as

$$(\mathbf{M} + \mathbf{M}_a)\ddot{\mathbf{u}} + (\mathbf{C} + \mathbf{C}_a)\dot{\mathbf{u}} + \mathbf{K}\mathbf{u} = \mathbf{F}_{ts} - (\mathbf{M} + \mathbf{M}_a)\mathbf{I}_z\ddot{g}_z(t) - \mathbf{C}_a\mathbf{I}_z\dot{g}_z(t) \quad (113)$$

where \mathbf{M}_a and \mathbf{C}_a are the additional mass and hydrodynamic damping matrices due to hydrodynamic effects. They can be obtained by assembling the additional element mass and hydrodynamic damping matrices as

$$\mathbf{M}_a = \sum_e^{\text{cantilever}} \mathbf{m}_a^e \quad (114)$$

$$\mathbf{C}_a = \mathbf{C}_\infty + \mathbf{C}_s = \sum_e^{\text{cantilever}} (\mathbf{c}_\infty^e + \mathbf{c}_s^e). \quad (115)$$

Here, \mathbf{m}_a^e is the additional element mass matrix, \mathbf{c}_∞^e is the additional element damping matrix when the beam is in free liquid, and \mathbf{c}_s^e is the additional element damping matrix due to the fluid squeezed in and out of the region between the cantilever and sample surface. They are obtained by

$$\mathbf{m}_a^e = \int_0^{L_e} \rho_a \mathbf{A} \mathbf{N}^T \mathbf{N} dx \quad (116)$$

$$\mathbf{c}_\infty^e = \int_0^{L_e} c_\infty \mathbf{N}^T \mathbf{N} dx \quad (117)$$

$$\mathbf{c}_s^e = \int_0^{L_e} \frac{\eta b^3}{h(x)^3} \mathbf{N}^T \mathbf{N} dx \quad (118)$$

where \mathbf{N} is the shape function vector for beam elements, ρ_a is the additional mass density, c_∞ is the hydrodynamic damping

when the cantilever is vibrating in free liquid, and c_s is the hydrodynamic damping due to the fluid squeezed in and out of the region between the cantilever and sample surface.

The additional mass density ρ_a can be calculated by (Rankl *et al* 2004)

$$\rho_a = 0.6\rho_{liq}L^{1/2}b^{3/2} \quad (119)$$

where ρ_{liq} is the mass density of the liquid in which the cantilever is immersed.

By representing an AFM cantilever as a string of beads, Hosaka *et al* (1995) expressed c_∞ and c_s by

$$c_\infty = 3\pi\eta + \frac{3}{4}\pi b\sqrt{2\rho_{liq}\eta\omega} \quad (120)$$

$$c_s = \frac{\eta b^3}{h(x,t)^3} \quad (121)$$

in which η is the viscosity of the liquid, ω is the vibrating circular frequency of the cantilever, and $h(x,t)$ is the transient distance between the cantilever and surface. Refer to figure 23; we have

$$h(x,t) = D + l \cos \alpha + (L - x) \sin \alpha + w(x,t) \cos \alpha. \quad (122)$$

4.2.3. Simulations and results. TM frequency and transient response analyses in liquid can be obtained by solving equation (113) (Song and Bhushan 2007). Figure 24 shows the simulated time histories of an AFM cantilever's vertical displacement and rotation in air as the tip-sample separation decreases with a constant velocity of $4.37 \times 10^{-4} \text{ m s}^{-1}$ from the initial separation of 210 nm. The driving frequency is at the first resonance frequency of the cantilever (43.7 kHz), and the excitation amplitude is $h_g = 3.84 \text{ nm}$. As we mentioned earlier, the AFM detecting system actually measures the cantilever rotation angle instead of the vertical displacement. Therefore, it is the time history of rotation $-\theta_y^C$ (figure 24(b)) that is directly comparable to the tip-sample approach curves shown in figure 22(b). Figure 24 clearly shows that before the tip taps on the surface (point A) the cantilever oscillates at constant amplitude. Between points A and B, cantilever amplitude decreases linearly as the tip approaches close to the surface. From point B on, the tip stays on the surface due to large adhesion (refer to figure 24(a)) but there is still some visible rotational oscillation (refer to figure 24(b)). Figure 24(b) demonstrates exactly the same characteristics as the measured result in figure 22(b).

The simulated time histories of d_z^C and $-\theta_y^C$ in liquid are shown in figure 25. In the simulation, the driving frequency is 33.0 kHz and the excitation amplitude is $h_g = 11.7 \text{ nm}$. The tip-sample separation is initially 20 nm and then decreases with a constant velocity of $3.3 \times 10^{-5} \text{ m s}^{-1}$. Figure 25(b) agrees very well with the experimental measurement in figure 22(c). Left to point A, the cantilever vibrates at a constant amplitude. After point A, the tip taps on the surface. Between point A and B, as the tip-sample separation gets smaller, the bottom envelope of the oscillation decreases (not quite linearly) but the upper envelope remains almost unchanged. After point B, the vibration amplitude again

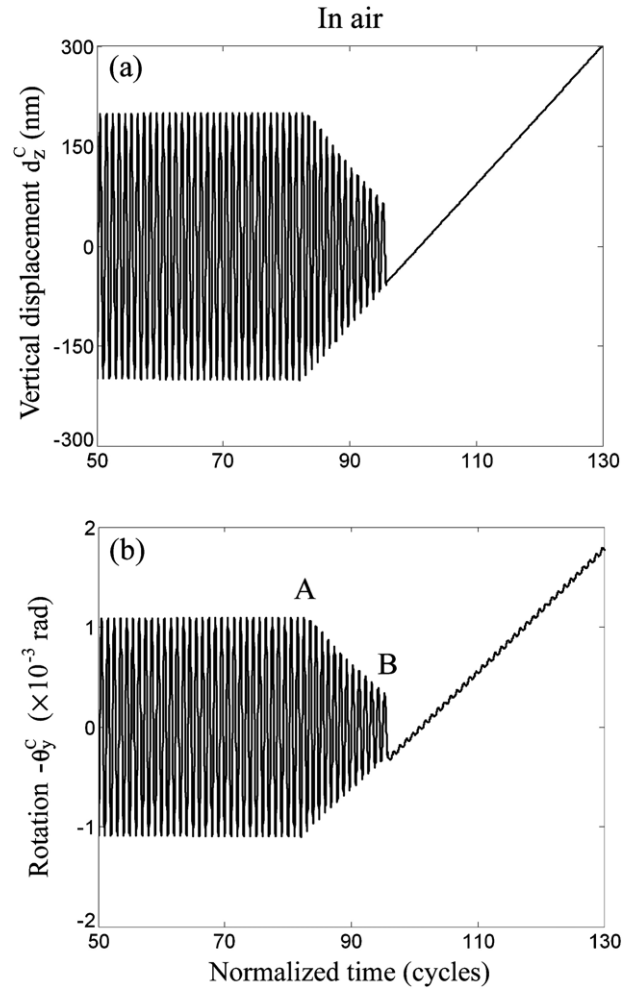


Figure 24. Simulated time histories of cantilever vertical displacement d_z^C (a) and rotation $-\theta_y^C$ (b) in air. The driving frequency is 43.7 kHz and the excitation amplitude is $h_g = 3.84 \text{ nm}$. The tip-sample separation is initially 210 nm and then decreases with a constant velocity of $4.37 \times 10^{-4} \text{ m s}^{-1}$. The Hamaker constant is $H = 7.4 \times 10^{-18} \text{ J}$ (Song and Bhushan 2007).

becomes constant. The pivoting motion of the cantilever when the tip is in contact with the surface is clearly shown in the lower part of figure 25(b). From figure 25(a), we can see that the cantilever tip does not stick to the surface until the sample surface is at the upper envelope of the oscillation. This is different from the observation in air. In air, with large adhesion, the tip sticks to the surface at a nonzero equilibrium tip-sample separation. This different behavior is due to the small adhesion force in liquid, and most importantly the hydrodynamic force that resists the cantilever to get close to the surface.

5. Quantitative evaluation of sample's mechanical properties

One very desirable application of AFM is to quantitatively evaluate a sample's mechanical properties. In dynamic modes, cantilever dynamic characteristics, including contact resonance frequency, vibration amplitude and phase angle, are related to the tip-sample interactions, which are functions of

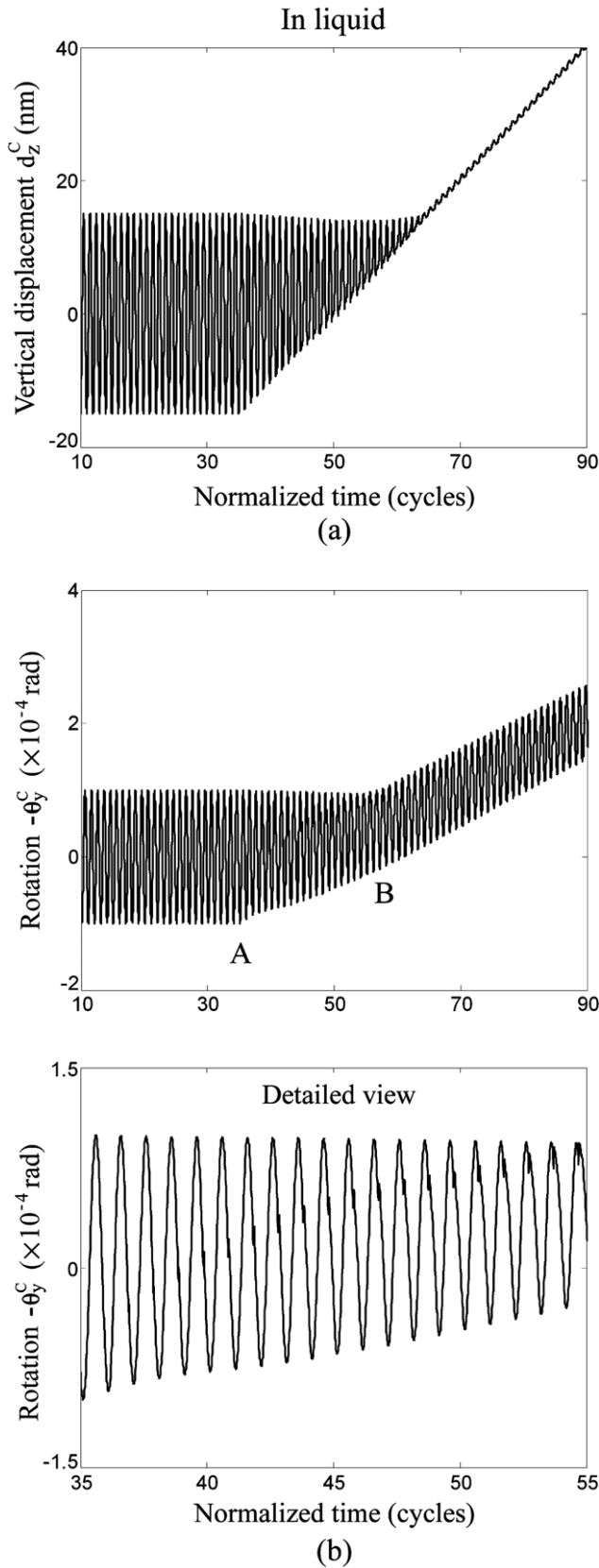


Figure 25. Simulated time histories of cantilever vertical displacement d_z^C (a) and rotation $-\theta_y^C$ (b) in liquid. The driving frequency is 33.0 kHz and the excitation amplitude is $h_g = 11.7$ nm. The tip-sample separation is initially 20 nm and then decreases with a constant velocity of 3.3×10^{-5} m s $^{-1}$. The Hamaker constant is $H = 2.96 \times 10^{-20}$ J (Song and Bhushan 2007).

the sample's material properties. Therefore, it is possible to evaluate a sample's material properties by measuring the cantilever's dynamic parameters during operation if the relations between cantilever responses and tip-sample interaction are known.

The contact stiffnesses in the normal and lateral directions k_n and k_{lat} are given in equations (3) and (4). If one can measure k_n and k_{lat} , E^* and G^* can be obtained. The material parameters of the tip (E_t , G_t , and ν_t) are known. The elastic and shear moduli, and Poisson's ratio of the sample, can then be calculated utilizing the following relations:

$$E^* = [(1 - \nu_t^2)/E_t + (1 - \nu_s^2)/E_s]^{-1} \quad (123)$$

$$G^* = [(2 - \nu_t)/G_t + (2 - \nu_s)/G_s]^{-1} \quad (124)$$

$$G_s = \frac{E_s}{2(1 + \nu_s)}. \quad (125)$$

In AFAM, the characteristic equation to calculate the contact resonance frequency of vertical bending (ω_c) can be obtained following the method described in section 2.3. With the normal contact viscosity being neglected ($\eta_n = 0$) and assuming that the tip is located at the end of the cantilever ($\lambda = 1$), the characteristic equation is

$$(\beta_w L)^3 [1 + \cos(\beta_w L) \cosh(\beta_w L)] + \frac{k_n}{EI_y/L^3} [\cosh(\beta_w L) \sin(\beta_w L) - \cos(\beta_w L) \sinh(\beta_w L)] = 0 \quad (126)$$

$$\beta_w^4 = \frac{\rho A}{EI_y} \omega_c^2. \quad (127)$$

Once ω_c is measured, from equation (126), the normal contact stiffness can be obtained by (Yamanaka and Nakano 1996, Rabe *et al* 1996)

$$k_n = -\frac{EI_y}{L^3} \frac{(\beta_w L)^3 [1 + \cos(\beta_w L) \cosh(\beta_w L)]}{[\cosh(\beta_w L) \sin(\beta_w L) - \cos(\beta_w L) \sinh(\beta_w L)]}. \quad (128)$$

In TR and LE mode, under a certain normal load f_c , the lateral contact stiffness can be calculated from the characteristic equation (41) (Song and Bhushan 2006a)

$$k_{lat} = \frac{GJ\beta_\theta}{l^2} \{\tan[\beta_\theta(1 - \lambda)L] - 1/\tan(\beta_\theta\lambda L)\} \quad (129)$$

$$\beta_\theta^2 = \frac{\rho I_P}{GJ} \omega_c^2. \quad (130)$$

Here ω_c represents the torsional contact resonance frequency. Since equation (41) is obtained from the pure torsional analysis, equation (129) can be used only if the pure torsional approximation is valid.

The lateral viscosity η_{lat} is related to the energy dissipated due to the tip-sample interaction (Song and Bhushan 2006c). For TR mode

$$E_{dis} = \pi \eta_{lat} \Omega [l^2 |\Theta_c|^2 + |\phi_v(x = L)|^2 + 2l |\Theta_c| |\phi_v(x = L)| \cos(\varphi_1 - \varphi_2)] \quad (131)$$

and for LE mode

$$E_{dis} = \pi \eta_{lat} \Omega [g_0^2 + l^2 |\Theta_c|^2 + |\phi_v(x = L)|^2 + 2l |\Theta_c| |\phi_v(x = L)| \cos(\varphi_1 - \varphi_2)]. \quad (132)$$

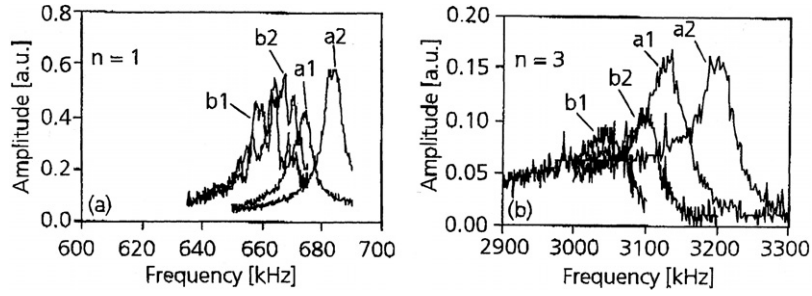


Figure 26. Experimental contact resonance spectra of a cantilever with a silicon tip. The sample is Si(100) with RF-sputtered coating of thickness 5 nm. The first (a) and third (b) flexural resonances were detected. The contact resonance spectra b1 and b2 were measured under two static normal loads, 410 nN and 820 nN, respectively. The contact resonance spectra a1 and a2 were obtained after two series of AFAM measurements under two static normal loads 410 nN and 820 nN, respectively (Amelio *et al* 2001).

Here, φ_1 and φ_2 are the phase angles of cantilever responses Θ_c and $\phi_v(x=L)$, respectively.

In TR mode, if k_{lat} is known, η_{lat} can be obtained using the measured phase shift (Song and Bhushan 2005)

$$\eta_{lat} = \{I_a k_{lat} l^2 [e^{2R_a L} s_1 - s_2] + (k_{lat} l^2 R_a - G J r_1) s_4 - (k_{lat} l^2 R_a + G J r_1) e^{2R_a L} s_3\} \times \{R_a l^2 \Omega [e^{2R_a L} s_1 - s_2] + I_a l^2 \Omega [e^{2R_a L} s_3 - s_4]\}^{-1}. \quad (133)$$

Here, it is assumed $\lambda = 1$, $s_1 = \cos(\phi + I_a L)$, $s_2 = \cos(\phi - I_a L)$, $s_3 = \sin(\phi + I_a L)$, $s_4 = \sin(\phi - I_a L)$, and R_a and I_a are the real and imaginary parts of the complex number a_{tr} . Again, equation (133) can only be applied if the pure torsional approximation is valid.

Unlike the pure torsional analysis, the coupled torsional–bending analysis of TR and LE mode could not lead to the explicit relations between the lateral contact stiffness/viscosity and cantilever torsional amplitude/phase shift, due to the mathematical complexity. In the case where pure torsional analysis cannot provide a good approximation for the cantilever torsional response, parameter identification methods, e.g. curve fitting, are needed for the extraction of a sample’s mechanical properties.

Geometry and material properties of the cantilever and tip are required to calculate the contact stiffness, viscosity and sample elastic parameters using equations (3), (4), (128), (129) and (133). In experiments, there are practical problems that make the reliable quantitative measurement difficult. AFM cantilevers may not behave perfectly like a clamped beam. It is difficult to obtain precisely the geometric dimensions and elastic constants of the cantilever and tip. Figure 26 shows an example of contact resonances of a cantilever measured in AFAM experiments (Amelio *et al* 2001). After two series of measurements, different contact spectra were detected. It is believed that the silicon tip radius was changed after successive experiments, as shown in figure 27 (Amelio *et al* 2001). The increase of the tip radius is caused by tip wear. Consequently, the measured contact stiffness and contact resonance frequency increase.

In the cases where the geometry and material parameters of the cantilever are not known precisely, reference measurements on samples with a known elastic constant may be used to derive the contact stiffness of interest without needing any cantilever information except the tip radius

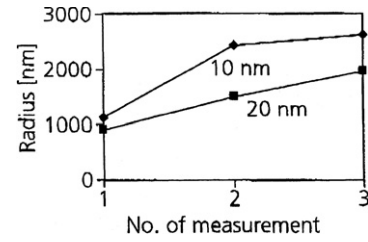


Figure 27. Increase of the tip radius after successive AFAM measurements on a sample of Si(100) with RF-sputtered coating of thickness 5 nm (Amelio *et al* 2001).

(Rabe *et al* 1996). Using equation (128), the normal contact stiffness of the sample of interest can be calculated by

$$k_n = k_n^{ref} \frac{\Phi(\beta_w L)}{\Phi(\beta_w^{ref} L)} \quad (134)$$

$$\Phi(x) = \frac{x^3 [1 + \cos x \cosh x]}{[\cosh x \sin x - \cos x \sinh x]} \quad (135)$$

where k_n^{ref} can be obtained from equation (3) given the normal load and tip radius. Using equation (128), $\beta_w L$ can be determined from

$$(\beta_w L)^4 = \frac{\omega_c^2 (\beta_w^{ref} L)^4}{\omega_c^{ref2}} = \frac{\omega_c^2 (\beta_w^{free} L)^4}{\omega_{free}^2} \quad (136)$$

where ω_{free} is the measured resonance frequency of the cantilever in free vibration and $\beta_w^{free} L$ is the mode constant of the clamped–free beam, which is determined from the characteristic equation.

6. Closure

This survey paper reviews the recent developments in modeling and applications of AFM dynamic modes. In the past two decades, with the wide use of AFM in nano-scale surface measurements and the quick development of innovative AFM dynamic modes, a good understanding of AFM cantilever dynamic behavior under tip–sample interaction in various environments (vacuum, air, liquid) became imminent and necessary for explaining AFM scanning images, improving

measurement techniques and evaluating a sample's material properties. For this purpose, numerous analytical and FE models have been developed to investigate surface-coupled cantilever dynamics in different AFM dynamic modes. With these analytical models, researchers have been able to set up the relations of cantilever response to tip–cantilever interaction for some of the AFM dynamic modes. These derived relations provide methods for the quantitative evaluation of a sample's mechanical properties. Using FE models, researchers are able to simulate and gain insights into the complex cantilever behavior in, e.g., the FFM profiling process and TM operated in liquid.

The ultimate goal of AFM-related research is to develop AFM instruments and techniques that are capable of quantitatively measuring samples' surfaces properties. Although there is still a long way to go, we certainly believe that a full understanding and exploitation of the rich dynamics of AFM cantilevers will provide us with prerequisites to achieve this goal.

References

- Albrecht T R, Grütter P, Horne D and Rugar D 1991 Frequency modulation detection using high- Q cantilevers for enhanced force microscopy sensitivity *J. Appl. Phys.* **69** 668–73
- Albrecht T R and Quate C F 1987 Atomic resolution imaging of a nonconductor by atomic force microscopy *J. Appl. Phys.* **62** 2599–602
- Amelio S, Goldade A V, Rabe U, Scherer V, Bhushan B and Arnold W 2001 Measurements of elastic properties of ultra-thin diamond-like carbon coatings using atomic force acoustic microscopy *Thin Solid Films* **392** 75–84
- Arinero R and L  v  que G 2003 Vibration of the cantilever in force modulation microscopy analysis by a finite element model *Rev. Sci. Instrum.* **74** 104–11
- Bhushan B 2005 *Introduction to Nanotribology and Nanomechanics* (Heidelberg: Springer)
- Bhushan B 2007 *Springer Handbook of Nanotechnology* 2nd edn (Heidelberg: Springer)
- Bhushan B and Kasai T 2004 A Surface topography-independent friction measurement technique using torsional resonance mode in an AFM *Nanotechnology* **15** 923–35
- Bhushan B and Qi J 2003 Phase contrast imaging of nanocomposites and molecularly thick lubricant films in magnetic media *Nanotechnology* **14** 886–95
- Binnig G, Gerber Ch, Stoll E, Albrecht T R and Quate C F 1987 Atomic resolution with atomic force microscope *Europhys. Lett.* **3** 1281–6
- Burnham N A, Behrend O P, Oulevey F, Gremaud G, Gallo P-J, Gourdon D, Dupas E, Kulik A J, Pollock H M and Briggs G A D 1997 How does a tip tap? *Nanotechnology* **8** 67–75
- Butt H J and Jaschke M 1995 Calculation of thermal noise in atomic force microscopy *Nanotechnology* **6** 1–7
- Caron A, Rabe U and Reinst  dtler M 2004 Imaging using lateral bending modes of atomic force microscopy cantilevers *Appl. Phys. Lett.* **85** 6398–6400
- Chen G Y, Warmack R J, Huang A and Thundat T 1995 Harmonic response of near-contact scanning force microscopy *J. Appl. Phys.* **78** 1465–9
- Chen G Y, Warmack R J, Oden P I and Thundat T 1996 Transient response of tapping scanning force microscopy in liquids *J. Vac. Sci. Technol. B* **14** 1313–7
- Chen J, Workman R K, Sarid D and H  per R 1994 Numerical simulations of a scanning force microscope with a large-amplitude vibrating cantilever *Nanotechnology* **5** 199–204
- Chen N and Bhushan B 2005 Morphological, nanomechanical and cellular structural characterization of human hair and condition distribution using torsional resonance mode with an atomic force microscopy *J. Microsc.* **220** 96–112
- Cleveland J P, Anczykowski B, Schmid A E and Elings V B 1998 Energy dissipation in tapping-mode atomic force microscopy *Appl. Phys. Lett.* **72** 2613–5
- Derjaguin B V, Muller V M and Toporov Y P 1975 Effect of contact deformations on the adhesion of particles *J. Colloid Interface Sci.* **53** 314–26
- Drake B, Prater C B, Weisenhorn A L, Gould S A C, Albercht T R, Quate C F, Cannell D S, Hansma H G and Hansma P K 1989 Imaging crystals, polymers, and processes in water with the atomic force microscope *Science* **243** 1586–9
- Dupas E, Gremaud G, Kulik A and Loubet J L 2001 High-frequency mechanical spectroscopy with an atomic force microscope *Rev. Sci. Instrum.* **72** 3891–7
- Fujisawa S, Yokoyama K, Sugawara Y and Morita S 1998 Analysis of experimental load dependence of two-dimensional atomic-scale friction *Phys. Rev. B* **58** 4909–16
- Garc  a R and P  rez R 2002 Dynamic atomic force microscopy methods *Surf. Sci. Rep.* **47** 197–301
- Giessibl F J 1995 Atomic resolution of the silicon (111)- 7×7 surface by atomic force microscopy *Science* **267** 68–71
- Giessibl F J 1997 Forces and frequency shifts in atomic-resolution dynamic-force microscopy *Phys. Rev. B* **56** 16010–5
- Goodman F O and Garcia N 1991 Roles of the attractive and repulsive forces in atomic force microscopy *Phys. Rev. B* **43** 4728–31
- Gorman D J 1975 *Free Vibration Analysis of Beams and Shafts* (New York: Wiley)
- Hansma H G, Vesenka J, Siegerist C, Kelderman G, Morrett H, Sinsheimer R L, Elings V, Bustamante C and Hansma P K 1992 Reproducible imaging and dissection of plasmid DNA under liquid with the atomic force microscope *Science* **256** 1180–4
- Hansma P K, Cleveland J P, Radmacher M, Walters D A, Hillner P E, Bezanilla M, Fritz M, Vie D and Hansma H G 1994 Tapping mode atomic force microscopy in liquids *Appl. Phys. Lett.* **64** 1738–40
- H  lscher H, Schwarz U D and Wiesendanger R 1996 Simulation of a scanned tip on a NaF(001) surface in friction force microscopy *Europhys. Lett.* **36** 19–24
- H  lscher H, Schwarz U D and Wiesendanger R 1997 Modelling of the scan process in lateral force microscopy *Surf. Sci.* **375** 395–402
- H  lscher H, Schwarz U D, Zw  rner O and Wiesendanger R 1998 Consequence of the stick–slip movement for the scanning force microscopy imaging of graphite *Phys. Rev. B* **57** 2477–81
- Hosaka H, Itao K and Kuroda S 1995 Damping characteristics of beam-shaped micro-oscillators *Sensors Actuators A* **49** 87–95
- Huang L and Su C 2004 A torsional resonance mode AFM for in-plane tip surface interfaces *Ultramicroscopy* **100** 277–85
- Hurley D C, Shen K, Jenett N M and Turner J A 2003 Atomic force acoustic microscopy methods to determine thin-film elastic properties *J. Appl. Phys.* **94** 2347–54
- Johnson K L 1985 *Contact Mechanics* (Cambridge: Cambridge University Press)
- Johnson K L, Kendall K and Roberts A D 1971 Surface energy and the contact of elastic solids *Proc. R. Soc. A* **324** 301–13
- Johnson K L and Woodhouse J 1998 Stick–slip motion in the atomic force microscopy *Tribol. Lett.* **5** 155–60
- Kasai T, Bhushan B, Huang L and Su C 2004 Topography and phase imaging using the torsional resonance mode *Nanotechnology* **15** 731–42
- Kitamura S and Iwatsuki M 1995 Observation of silicon surfaces using ultrahigh-vacuum noncontact atomic force microscopy *Japan. J. Appl. Phys.* **35** L668–71
- Lee S I, Howell S W, Raman A and Reifengerger R 2002 Nonlinear dynamics of microcantilevers in tapping mode atomic force

- microscopy: a comparison between theory and experiment *Phys. Rev. B* **66** 115409
- Maivald P, Butt H J, Gould S A C, Prater C B, Drake B, Gurley J A, Elings V B and Hansma P K 1991 Using force modulation to image surface elasticities with the atomic force microscopy *Nanotechnology* **2** 103–6
- Marti O, Colchero J and Mlynek J 1990 Combined scanning force and friction microscopy of mica *Nanotechnology* **1** 141–4
- Marti O, Drake B and Hansma P K 1987 Atomic force microscopy of liquid-covered surfaces: atomic resolution images *Appl. Phys. Lett.* **51** 484–6
- Mate C M, McClelland G M, Erlandsson R and Chiang S 1987 Atomic-scale friction of a tungsten tip on a graphite surface *Phys. Rev. Lett.* **59** 1942–5
- Meyer G and Amer N 1990 Simultaneous measurement of lateral and normal forces with an optical-beam-deflection atomic force microscopy *Appl. Phys. Lett.* **57** 2089–91
- Mizes H A, Park S I and Harrison W A 1987 Multiple-tip interpretation of anomalous scanning-tunneling-microscopy images of layered materials *Phys. Rev. B* **36** R4491–4
- MultiMode™ SPM Instructor Manual 1997 *Version 4.31ce* Digital Instruments, Santa Barbara, CA
- Putman C A J, van der Werf K O, De Grooth B G, van Hulst N F and Greve J 1994 Tapping mode atomic force microscopy in liquid *Appl. Phys. Lett.* **64** 2454–6
- Rabe U, Amelio S, Kester E, Scherer V, Hirsekorn S and Arnold W 2000 Quantitative determination of contact stiffness using atomic force acoustic microscopy *Ultrasonics* **38** 430–7
- Rabe U, Amelio S, Kopycinska M, Hirsekorn S, Kempf M, Göken M and Arnold W 2002 Imaging and measurement of local mechanical material properties by atomic force acoustic microscopy *Surf. Interface Anal.* **33** 65–70
- Rabe U and Arnold W 1994 Acoustic microscopy by atomic force microscopy *Appl. Phys. Lett.* **64** 1493–5
- Rabe U, Janser K and Arnold W 1996 Vibrations of free and surface-coupled atomic force microscope cantilevers: theory and experiment *Rev. Sci. Instrum.* **67** 3281–93
- Rabe U, Turner J and Arnold W 1998 Analysis of the high-frequency response of atomic force microscope cantilevers *Appl. Phys. A* **66** S277–82
- Rankl C, Pastushenko V, Kienberger F, Stroh C M and Hinterdorfer P 2004 Hydrodynamic damping of a magnetically oscillated cantilever close to a surface *Ultramicroscopy* **100** 301–8
- Reinstädler M, Kasai T, Rabe U, Bhushan B and Arnold W 2005a Imaging and measurement of elasticity and friction using the TR mode *J. Phys. D: Appl. Phys.* **38** R269–82
- Reinstädler M, Rabe U, Goldade A, Bhushan B and Arnold W 2005b Investigating ultra-thin lubricant layers using resonant friction force microscopy *Tribol. Int.* **38** 533–41
- Reinstädler M, Rabe U, Scherer V, Hartmann U, Goldade A, Bhushan B and Arnold W 2003 On the nanoscale measurement of friction using atomic-force microscope cantilever torsional resonances *Appl. Phys. Lett.* **82** 2604–6
- Ruan J and Bhushan B 1994 Atomic-scale and microscale friction studies of graphite and diamond using friction force microscopy *J. Appl. Phys.* **76** 5022–35
- Sader J E 1998 Frequency response of cantilever beams immersed in viscous fluids with applications to the atomic force microscopy *J. Appl. Phys.* **84** 64–76
- Sader J E 2003 Susceptibility of atomic force microscope cantilevers to lateral force *Rev. Sci. Instrum.* **74** 2438–43
- Sader J E and Sader R C 2003 Susceptibility of atomic force microscope cantilevers to lateral force: experimental verification *Appl. Phys. Lett.* **83** 3195–7
- San Paulo A and García R 2001 Tip-surface forces, amplitude, and energy dissipation in amplitude-modulation (tapping mode) force microscopy *Phys. Rev. B* **64** 193411
- Sasaki N, Kobayashi K and Tsukada M 1996 Atomic-scale friction image of graphite in atomic-force microscopy *Phys. Rev. B* **54** 2138–49
- Scherer V, Arnold W and Bhushan B 1999 Lateral force microscopy using acoustic friction microscopy *Surf. Interface Anal.* **27** 578–87
- Scott W W and Bhushan B 2003 Use of phase imaging in atomic force microscopy for measurement of viscoelastic contrast in polymer nanocomposites and molecularly-thick lubricant films *Ultramicroscopy* **97** 151–69
- Song Y and Bhushan B 2005 Quantitative extraction of in-plane surface properties using torsional resonance mode of atomic force microscopy *J. Appl. Phys.* **97** 083533
- Song Y and Bhushan B 2006a Dynamic analysis of torsional resonance mode of atomic force microscopy and its application to in-plane surface property extraction *Microsyst. Technol.* **12** 129–230
- Song Y and Bhushan B 2006b Simulation of dynamic modes of atomic force microscopy using a 3D finite element model *Ultramicroscopy* **106** 847–73
- Song Y and Bhushan B 2006c Coupling of lateral bending and torsion in torsional resonance and lateral excitation modes of atomic force microscopy *J. Appl. Phys.* **99** 094911
- Song Y and Bhushan B 2006d Atomic-scale topographic and friction force imaging and cantilever dynamics in friction force microscopy *Phys. Rev. B* **74** 165401
- Song Y and Bhushan B 2007 Finite-element vibration analysis of tapping-mode atomic force microscopy in liquid *Ultramicroscopy* **107** 1095–104
- Stark R W, Schitter G, Startk M, Guckenberger R and Stemmer A 2004 State-space model of freely vibrating and surface-coupled cantilever dynamics in atomic force microscopy *Phys. Rev. B* **69** 085412
- Tamayo J and García R 1998 Relationship between phase shift and energy dissipation in tapping-mode scanning force microscopy *Appl. Phys. Lett.* **73** 2926–8
- Turner J A 2004 Non-linear vibrations of a beam with cantilever-hertzian contact boundary conditions *J. Sound Vib.* **275** 177–95
- Turner J A, Hirsekorn S, Rabe U and Arnold W 1997 High-frequency response of atomic-force microscope cantilevers *J. Appl. Phys.* **82** 966–79
- Turner J A and Wiehn J S 2001 Sensitivity of flexural and torsional vibration modes of atomic force microscopy cantilevers to surface stiffness variations *Nanotechnology* **12** 322–30
- Wang L 1998 Analytical descriptions of the tapping-mode atomic force microscopy response *Appl. Phys. Lett.* **73** 3781–3
- Wang L 1999 The role of damping in phase imaging in tapping mode atomic force microscopy *Surf. Sci.* **429** 178–85
- Wright O B and Nishiguchi N 1997 Vibration dynamics of force microscopy: effect of tip dimensions *Appl. Phys. Lett.* **71** 626–8
- Yamanaka K and Nakano S 1996 Ultrasonic atomic force microscope with overtone excitation of cantilever *Japan. J. Appl. Phys.* **35** 3787–92
- Yamanaka K and Nakano S 1998 Quantitative elasticity evaluation by contact resonance in an atomic force microscopy *Appl. Phys. A* **66** S313–7
- Yamanaka K, Ogiso H and Kolosov O 1994 Ultrasonic force microscopy for nanometer resolution substrate imaging *Appl. Phys. Lett.* **64** 178–80
- Yamanaka K and Tomita E 1995 Lateral force modulation atomic force microscopy for selective imaging of friction force *Japan. J. Appl. Phys.* **34** 2879–82